

MECHANICAL BEHAVIOR OF ADDITIVELY MANUFACTURED
POLYMER COMPOSITE STRUCTURES AND INTERFACES

A THESIS SUBMITTED TO
THE GRADUATE SCHOOL OF NATURAL AND APPLIED SCIENCES
OF
MIDDLE EAST TECHNICAL UNIVERSITY

BY

MEHMET KEPENEKÇİ

IN PARTIAL FULFILLMENT OF THE REQUIREMENTS
FOR
THE DEGREE OF MASTER OF SCIENCE
IN
MECHANICAL ENGINEERING

SEPTEMBER 2021

Approval of the thesis:

**MECHANICAL BEHAVIOR OF ADDITIVELY MANUFACTURED
POLYMER COMPOSITE STRUCTURES AND INTERFACES**

submitted by **MEHMET KEPENEKCI** in partial fulfillment of the requirements
for the degree of **Master of Science in Mechanical Engineering, Middle East
Technical University** by,

Prof. Dr. Halil Kalıpçılar
Dean, Graduate School of **Natural and Applied Sciences** _____

Prof. Dr. M. A. Sahir Arıkan
Head of the Department, **Mechanical Engineering** _____

Assoc. Prof. Dr. Sezer Özerinç
Supervisor, **Mechanical Engineering, METU** _____

Examining Committee Members:

Assoc. Prof. Dr. Ulaş Yaman
Mechanical Engineering, METU _____

Assoc. Prof. Dr. Sezer Özerinç
Mechanical Engineering, METU _____

Prof. Dr. Demirkan Çöker
Aerospace Engineering, METU _____

Assoc. Prof. Dr. Hüsnü Dal
Mechanical Engineering, METU _____

Prof. Dr. Teyfik Demir
Mechanical Engineering, TOBB ETÜ _____

Date: 06.09.2021

I hereby declare that all information in this document has been obtained and presented in accordance with academic rules and ethical conduct. I also declare that, as required by these rules and conduct, I have fully cited and referenced all material and results that are not original to this work.

Name Last name : Mehmet Kepenekci

Signature :

ABSTRACT

MECHANICAL BEHAVIOR OF ADDITIVELY MANUFACTURED POLYMER COMPOSITE STRUCTURES AND INTERFACES

Kepenekci, Mehmet
Master of Science, Mechanical Engineering
Supervisor: Assoc. Prof. Dr. Sezer Özerinç

September 2021, 84 pages

Additive manufacturing (AM) is a technology based on the layer-by-layer production of parts. Fused filament fabrication (FFF) is one of the most cost-effective and popular AM techniques for the production of polymeric structures.

While the initial use of FFF was limited to thermoplastics such as PLA and ABS, recent advances enabled the printing of composite materials and structures for superior mechanical performance. Multi-material printing through dual-nozzle systems offers a unique opportunity towards this end, enabling the production of complex geometries composed of different types of polymers.

The first part of this thesis investigated one aspect of these composites – the mechanical behavior of the interfaces between two polymers. For this purpose, a range of PLA-TPU interfaces were produced by FFF, and the bonding between the two domains was investigated through mechanical testing and finite element modeling. The results demonstrated that the poor adhesion between the polymers can be significantly improved through the design of interlocking structures.

Another common approach to the printing of composite structures by FFF is the utilization of polymer-matrix filaments with reinforcements. Short carbon fiber reinforced polyamide (PA-CF) is among the most promising composite filaments

due to its excellent properties. While the mechanical characteristics of this specific composite have been widely studied, the corresponding performance of lightweight cellular structures made of PA-CF is not well known. The second part of this thesis investigated the mechanical performance of a wide range of cellular structures made of PA-CF through compression testing and high-speed imaging. The results show that cellular PA-CF structures provide a great combination of high strength and lightweight.

The findings of the thesis show that FFF-produced composites offer great potential for load-bearing applications in a wide range of industries. Further optimization of the polymer-polymer interfaces will enable the reliable application of multi-material printing in load-bearing applications. The additional characterization of the PA-CF cellular structures will focus on their impact performance and will further expand the applications of FFF technology towards the design and manufacturing of energy absorbing structures.

Keywords: Additive Manufacturing, 3D Printing, Fused Filament Fabrication, Carbon Fiber Reinforced Polymers, Elastomers

ÖZ

EKLEMELİ İMALAT İLE ÜRETİLEN POLİMER KOMPOZİT YAPILARIN VE ARAYÜZEYLERİN MEKANİK ÖZELLİKLERİ

Kepenekci, Mehmet
Yüksek Lisans, Makina Mühendisliği
Tez Yöneticisi: Doç. Dr. Sezer Özerinç

Eylül 2021, 84 sayfa

Eklemeli imalat (Eİ), katmanlı üretime dayanan bir üretim teknolojisidir. Eriyik yığıma modellemesi (EYM), plastik üretimi için en uygun maliyetli ve yaygın Eİ tekniklerinden birisidir.

EYM'nin önceki yıllardaki kullanımı PLA ve ABS gibi termoplastiklerle sınırlıyken, günümüzün filament teknolojileriyle beraber, üstün mekanik özelliklere sahip kompozit malzemelerin ve yapıların basılması mümkün hale gelmiştir. Çift nozullu sistemlerin sunduğu çok malzemeli baskı imkanı, farklı polimer türlerinden oluşan karmaşık geometrilerin üretilmesine olanak sağlamıştır.

Tezin ilk kısmında, yukarıda bahsedilen teknolojiler kapsamında, iki farklı polimer malzemenin arayüzeylerinin mekanik davranışı incelenmiştir. Bu amaçla, EYM yöntemi ile PLA ve TPU malzemeleri kullanılarak çeşitli yapılar üretilmiş ve bu iki malzeme arasındaki arayüzey dayanımı mekanik testler ve sonlu eleman modellemesi yöntemiyle incelenmiştir. Sonuçlar, polimer malzemeler arasındaki oldukça zayıf olan arayüzey dayanımının, iç içe geçmeli geometriler aracılığıyla önemli ölçüde artırılabilirliğini göstermiştir.

EYM ile kompozit yapıların üretimine yönelik bir diğer yaklaşım ise katkılı polimer filamentlerin kullanılmasıdır. Kısa karbon fiber takviyeli poliamid (PA-CF), üstün

mekanik özellikleri nedeniyle gelecek vaat eden kompozit filamentler arasındadır. Bu kompozitin mekanik özellikleri literatürde detaylı olarak çalışılmış olsa da, PA-CF filament kullanılarak üretilmiş hafif hücresel yapıların performansı bilinmemektedir. Tezin ikinci kısmında, basma testleri ve yüksek hızlı görüntüleme yoluyla PA-CF malzeme ile üretilmiş çeşitli hücresel yapıların mekanik performansı araştırılmıştır. Sonuçlar, hücresel PA-CF yapılarının, yüksek dayanım ve hafifliği aynı anda sağladığını göstermektedir.

Bu tezde EYM yöntemi ile üretilmiş kompozit yapıların mekanik davranışının çeşitli yönleri araştırılmıştır. Deneysel veriler ve sonlu elemanlar yöntemi öngörülerini EYM yöntemi ile üretilen kompozitlerin çeşitli endüstriyel uygulamalar için büyük bir potansiyele sahip olduğunu göstermektedir. Bu yapıların arayüzey optimizasyonu ve darbe dayanımına ilişkin gelecekte yapılacak olan ilave çalışmalar, EYM üretim teknolojisinin yapısal malzeme alanındaki uygulamalarını artıracaktır.

Anahtar Kelimeler: Eklemeli İmalat, 3B Baskı, Eriyik Yığılma Modellemesi, Karbon Fiber Takviyeli Polimerler, Elastomerler

To My Wife and My Family

ACKNOWLEDGMENTS

I would like to thank my thesis supervisor Assoc. Prof. Dr. Sezer Özerinç for his guidance and encouragement throughout my master's study. I am sincerely grateful to him for his invaluable recommendations that help me to plan my academic studies.

I would like to thank Assoc. Prof. Dr. Ulaş Yaman for his helpful comments and guidance, and to Bahar Gharehpapagh for her collaboration regarding the second part of my thesis.

I want to thank Servet Şehirli as he shared his experiences and help without hesitation. I also want to thank my colleagues in the Nanomechanics Laboratory, especially Burçin Kaygusuz, Roozbeh Neshani, Sencer Aydın, Ali Bagheri Behboud, and my former colleague Mohammad Abboud for their friendship. I am thankful to them as I learned a lot from the fruitful discussions that we had.

I want to thank the METU Central Laboratory staff, especially Ali Güzel, for their help and cooperation.

Lastly, I would like to thank my wife, Aybike, for her endless support and encouragement during my studies. I am grateful to my family for motivating me throughout the thesis work.

This thesis study was partly supported by The Scientific and Technological Research Council of Turkey (TÜBİTAK) through the 3501 project with grant #116M429.

TABLE OF CONTENTS

ABSTRACT.....	v
ÖZ	vii
ACKNOWLEDGMENTS	x
TABLE OF CONTENTS.....	xi
LIST OF TABLES	xiv
LIST OF FIGURES	xv
LIST OF ABBREVIATIONS	xix
LIST OF SYMBOLS	xx
CHAPTERS	
1 INTRODUCTION	1
1.1 Additive Manufacturing.....	3
1.2 Fused Filament Fabrication (FFF).....	3
1.2.1 Enclosure Types	6
1.2.2 Extruder Placement Types	6
1.2.3 Table and Printhead Movement	6
1.3 Multi-material FFF	7
1.3.1 Single Nozzle	7
1.3.2 Multiple Nozzle	8
1.3.3 Multi-Material Interfaces	8
1.3.3.1 Finite Element Modeling (FEM) of Interfaces.....	9
1.4 Materials Used in FFF	9
1.4.1 Acrylonitrile Butadiene Styrene (ABS).....	11
1.4.2 Polylactic Acid (PLA).....	11

1.4.3	Thermoplastic Polyurethane (TPU).....	12
1.4.4	Polyamide (PA)	12
1.4.5	Carbon Fiber Reinforced Polymers	13
1.4.5.1	Carbon Nanotube (CNT) Additions.....	13
1.4.5.2	Continuous CF Additions	13
1.4.5.3	Chopped CF Additions	14
1.5	Infill Patterns Used in FFF	15
1.6	Thesis Work	15
2	ELASTOMER-PLA INTERFACES PRODUCED BY FFF	17
2.1	Introduction	17
2.2	Experimental Details	17
2.2.1	Sample Geometries.....	18
2.2.2	Sample Preparation.....	20
2.2.2.1	3D CAD Modeling and Toolpath Creation.....	20
2.2.2.2	3D Printing.....	20
2.2.3	Mechanical Testing	23
2.2.4	Finite Element Modeling	25
2.3	Results and Discussion.....	29
2.3.1	Experimental Results	29
2.3.2	FEM Results	38
2.4	Conclusions	43
3	CARBON FIBER-REINFORCED POLYAMIDE CELLULAR STRUCTURES PRODUCED BY FFF	45
3.1	Introduction	45

3.2	Experimental details	46
3.2.1	Sample Preparation	46
3.2.2	Uniaxial Tensile Testing	46
3.2.3	Compressive Testing.....	47
3.2.3.1	Energy Absorbance Efficiency.....	50
3.3	Results and Discussion	53
3.3.1	Tensile Testing.....	53
3.3.2	Compressive Testing.....	59
3.3.3	Energy Absorption and Efficiency.....	63
3.4	Conclusions	69
4	CONCLUSIONS AND FUTURE WORK	71
	REFERENCES	73

LIST OF TABLES

TABLES

Table 2.1. FFF 3D printing parameters for PLA, TPU, and interface specimens. .	22
Table 3.1. FFF 3D printing parameters of compressive test specimens printed with PA and PAHT CF15 materials	46
Table 3.2. The compressive modulus, compressive yield strength, and maximum energy absorption efficiency values of the different compressive test specimens.....	66

LIST OF FIGURES

FIGURES

Figure 1.1. Schematic illustration of a typical FFF 3D printer [23].	4
Figure 1.2. Market share of the FFF 3D printing filaments [54].	10
Figure 2.1. Tensile test specimens (a) PLA (b) TPU (c) Shear Test (d) Combed. Comb length is given as "x" in the drawing, which was used as 0, 2, 4, and 6 mm in this project. The thickness of (a), (c), and (d) is 3.2mm, and (b) is 1.6 mm.	19
Figure 2.2. Flashforge Creator Pro dual nozzle FFF 3D printer.	21
Figure 2.3. 3D printed PLA and TPU dogbone specimens. (i) PLA specimen was printed using Ultrafuse blue PLA filament, and the. (ii) TPU specimen was printed using Ultrafuse TPU 85A filament. The <i>P</i> in the naming indicates that the material is PLA, and <i>T</i> indicates that the material is TPU.....	22
Figure 2.4. Flat interface specimen (TP0) (i), shear test specimen (ii), and combed specimens having (iii) 2 mm (iv) 4 mm (v) 6 mm comb lengths. Blue parts are printed with PLA and white parts with TPU filament.	23
Figure 2.5. The screenshot showing the boundary conditions used in the simulations of PLA and TPU specimens.	27
Figure 2.6. Screenshot of discretized flat interface specimen, half of the specimen was modeled using symmetry boundary conditions.	28
Figure 2.7. Screenshot of the discretized tensile shear test specimen, half of the specimen is modeled using symmetry boundary conditions.....	29
Figure 2.8. Fractured PLA tensile test specimen after the uniaxial tensile test.	29
Figure 2.9. Fractured TPU tensile test specimen after the uniaxial tensile test.	30
Figure 2.10. The photographs of multi-material specimens after the uniaxial tensile tests. The flat interface (i), shear test specimen (ii), and	

combed specimens having (iii) 2 mm (iv) 4 mm (v) 6 mm comb lengths.....	31
Figure 2.11. Tensile test results of TPU-PLA multi-material interface specimens.....	32
Figure 2.12. Displacement at fracture of the comb interface specimens having 0, 2, 4, and 6 mm comb lengths.....	33
Figure 2.13. Effective stress versus tensile deformation response of the combed specimens having 0, 2, 4, and 6 mm comb lengths. The insets are (i) stress versus percent elongation graph of the PLA tensile test specimen and (ii) stress versus percent elongation graph of the TPU specimen.	34
Figure 2.14. Stress versus elongation diagram of the shear stress test specimens. Shearing stress is calculated using the total interfacial area. The elongation value shows the total tensile elongation of the tensile test specimen in the gage length.....	35
Figure 2.15. The snippets from the tensile test video of the multi-material shear tensile test specimen. The blue markings are drawn with a pen for alignment and to use in the post-processing of the video.....	36
Figure 2.16. The snapshots from the tensile test video of the multi-material combed tensile test specimen with a comb length of 6 mm.	37
Figure 2.17. Optical microscopy image of a fractured interface of TPU part of the dogbone tensile shear test specimen.	38
Figure 2.18. The tensile test result versus simulation result graph for (a) PLA and (b) TPU specimens.....	39
Figure 2.19. (a) The Von-Mises stress state of the flat interface specimen just before the crack initiation (b) Snippets showing the progression of the cohesive contact loss at interface surface of the TPU specimen. The red regions show a bonded contact, and the blue regions indicate those not in contact.	41
Figure 2.20 Tensile test result versus simulation result graph for TP0 specimen...	42

Figure 2.21. Tensile test result versus simulation result graph for the shear test specimen.....	43
Figure 3.1. Tensile test specimens printed with PA and PAHT CF15 filament and having 0°, 90° raster angles, and a concentric infill.....	47
Figure 3.2. The compressive specimens printed with PA and PAHT CF15 filaments. The upper five specimens were printed with PA, and the specimens at the bottom were printed using PAHT CF15 material. The corresponding geometries are hexagonal with a wall, hexagonal without a wall, Voronoi, gyroid with a wall, and gyroid without wall from left to right and top to bottom, respectively.	49
Figure 3.3. Stress versus strain response of an ideal energy absorber.	51
Figure 3.4. Absorbed energy per unit volume versus peak stress diagram of an ideal energy absorber.	52
Figure 3.5 Absorbed energy efficiency versus compressive strain graph for an ideal energy absorber.	53
Figure 3.6. Tensile stress versus tensile strain plot of PAHT CF15 specimens for concentric infill, 0°, and 90° raster angles.	54
Figure 3.7. Tensile test results of PA specimen tensile test specimens, for concentric infill, 0°, and 90° raster angles.	55
Figure 3.8. The optical microscopy image showing the top surface of a concentric infill tensile test specimen.	56
Figure 3.9. The fractured tensile test specimens printed with PAHT CF15 and having 0°, 90° raster angles, and a concentric infill.....	57
Figure 3.10. Tensile modulus, ultimate tensile strength, and tensile strain at fracture values of the PA and PAHT CF15 specimens for concentric infill, 0°, and 90° raster angles.	58
Figure 3.11. Compressive test results of the honeycomb (black), gyroid (gray), and Voronoi (red) infill patterns for both PA and PAHT CF15 specimens.	60

Figure 3.12. Compressive test results of (i) honeycomb, (ii) gyroid, (iii) Voronoi infill patterns for both PA and PAHT CF15 materials. 62

Figure 3.13. Peak stress versus absorbed energy per unit volume graph of compressive test specimens printed using (i) honeycomb, (ii) gyroid, and (iii) Voronoi infill with and without wall. 64

Figure 3.14. The compressive stress and absorbed energy efficiency versus strain plot of best and worst-performing specimens. The PA Voronoi specimen was printed without a wall, and the PA Honeycomb specimen was printed without a wall, shown on top and bottom, respectively. 67

Figure 3.15. The photographs of the (a) best and (b) worst performing specimens. These were taken from the test video shot during the compressive test. 68

LIST OF ABBREVIATIONS

ABBREVIATIONS

3D	Three Dimensional
ABS	Acrylonitrile Butadiene Styrene
CAD	Computer-Aided Design
CNT	Carbon Nanotube
CF	Carbon Fiber
CFRP	Carbon Fiber Reinforced Polymer
FDM	Fused Deposition Modeling
FFF	Fused Filament Fabrication
PA	Polyamide
PLA	Polylactic Acid
STL	Standard Triangle Language
TM	Traditional Manufacturing
TPE	Thermoplastic Elastomer
TPU	Thermoplastic Polyurethane
UTS	Ultimate Tensile Strength

LIST OF SYMBOLS

SYMBOLS

μm	Micrometers
F_T	Tensile force
F_C	Compressive force
A_C	Cross-sectional area
A_{shear}	Shearing area
$A_{comb,TPU}$	Cross-sectional area of TPU at comb region
E_C	Compressive modulus
σ_C	Compressive stress
σ_T	Tensile stress
σ_E	Effective stress
σ_{shear}	Shear stress
$\sigma_{comb,TPU}$	Stress in TPU at comb region
σ_p	Peak stress
σ_Y	Yield strength
ε	Strain
ε_y	Strain at the onset of yielding
ρ_{mat}	Mass density of the filament material
ρ_V	Volumetric density
m	Measured mass

m_{est}	Estimated mass of 100% infill specimen
V	Calculated volume using the part dimensions
W	Absorbed energy per unit volume
η	Energy absorption efficiency

CHAPTER 1

INTRODUCTION

Traditional manufacturing (TM) processes are primarily based on subtractive (e.g., milling, turning, drilling) or formative procedures (e.g., casting, forging), which are being utilized for producing the parts the mass-manufactured of the consumer goods and machine parts [1]. The limitations of the TM methods hindered the development of the new generation designs since producing parts with micron-level details and internal cavities are extremely costly, if not impossible. Since producing internal cavities with the TM method is a challenging task, there is material left in the produced part that does not bear any load, which increases the mass of the product and causes material waste [2].

On the other hand, there is more freedom in production possibilities in additive manufacturing (AM) which enabled the production of parts that were impossible to manufacture previously [3]. It is possible to manufacture a custom part solely designed to a calculated load case, such that all of the material in part are used as load-bearer sections; therefore, the weight of the products can be significantly lowered [4]. Weight reduction is essential to avoid wasting materials, and decreasing the weight of moving parts lowers the mass moment of inertia; therefore, the energy needed to accelerate or decelerate is lowered.

Also, it is viable to manufacture a product customized for each customer using AM [5], contrary to the TM methods. Therefore, the AM processes make it possible to produce parts more reliably and sustainably [6]. However, it should be noted that, as Attaran stated [7], the AM is not a replacement for TM but brings unique complementary features to the manufacturing processes.

A variety of material types can be manufactured through AM processes, such as stereolithography (SLA), selective laser sintering (SLS), selective laser melting (SLM), and fused filament fabrication (FFF) [8].

FFF, also known as Fused Deposition Modeling (FDM), is one of the most widely used AM polymer part fabrication methods. The simplicity of the method enables the availability of desktop printers, which makes FFF a cheap and easy to access technique. Filaments of polymer material are needed to manufacture parts through the FFF process. Even though many different thermoplastic polymer materials can be used in FFF, the most widely used polymer filaments are PLA and ABS. Due to their flexibility, one of the most noteworthy thermoplastic materials is the thermoplastic elastomer (TPE) filaments. Nano or fiber particles can be added to the polymer matrix to alter the mechanical, thermal, and electrical properties of the polymers. The fiber additions can be in continuous form or chopped from a continuous fiber in various lengths.

Some FFF printers can print multiple materials in a single part, which paves the way for novel scientific and technical findings [9]. There are two main methods of multi-material printing through the FFF method: single nozzle with multiple filament inlets and multi-nozzle setups.

There are two main FFF 3D printer types based on the filament feeding mechanisms: direct-drive and Bowden extruder, which have positive and negative qualities. While the extruder carrier assembly in direct-drive extruders is heavier and bulkier, the carrier assembly in Bowden extruders has a lower weight. Although it seems Bowden extruders are the right choice for FFF, for flexible filaments, it is customary to use a direct drive extruder as the filaments can buckle in the Bowden tube, which increases the friction between the tube and the filament and can result in clogging.

Throughout this thesis work, PLA, thermoplastic polyurethane (TPU), polyamide (PA), and carbon-fiber-reinforced polymer (CFRP) PA are used. A direct-drive dual-nozzle FFF 3D printer was used for printing the TPU and PLA parts, whereas a Bowden-extruder dual nozzle printer was utilized for printing PA and CFRP PA. For

mechanical characterization of the printed parts, uniaxial tensile and compressive tests are done.

1.1 Additive Manufacturing

As traditional manufacturing methods are primarily based on subtractive procedures, these processes limit the complexity level of the produced parts. On the other hand, additive manufacturing (AM) is an approach based on a layer-by-layer production of a part [10], which enables the production of parts with way more complex design compared to that could be achieved with traditional manufacturing methods [11,12].

Utilizing AM methods makes it possible to create solid and lightweight parts and reduce material cost and environmental impact. The flexibility introduced by the AM methods enabled the designers to use optimization methods, such as topology optimization, with fewer restrictions compared to TM methods [13–15].

While most of the time, mass production is needed for feasibility in traditional methods, it is easy to create custom parts in low quantities with AM [16]. Being able to create custom parts also allows producing machine spare parts that the manufacturer does not supply. In this way, the economic use time of a machine can be increased dramatically. Moreover, as the automation level increases in the industry, the mass customization need also increases, leading to the need to develop non-traditional production methods [17].

There are various AM methods, including fused filament fabrication (FFF), stereolithography (SLA), selective laser sintering (SLS), direct energy deposition (DED) [18,19]. These methods are used to manufacture ceramic, metallic, and polymeric materials with sub-millimeter [20] to several meters in sizes [21].

1.2 Fused Filament Fabrication (FFF)

Fused filament fabrication (FFF), also known as Fused deposition modeling (FDM), is one of the most popular and cost-effective AM techniques for custom-shaped plastic parts [22].

There are various FFF 3D printer types, but the printing process can be generalized, as shown in Figure 1.1 [23]. The printing process starts with a driving motor pulling the polymer filament to a hot end. The hot end melts the filament, and then a nozzle feeds the molten filament onto the printing platform. Print-head generates the required shape by moving in the XY plane. After the completion of a layer, the process repeats itself for the next one.

The layer-by-layer production on a flat building platform requires a support structure when the printed parts have overhanging sections [24]. These support structures may be printed using a single filament, or another material can be utilized and usually washed away with a solvent [25,26]. Thus, the parts printed with both methods require post-processing, which is sometimes highly tedious.

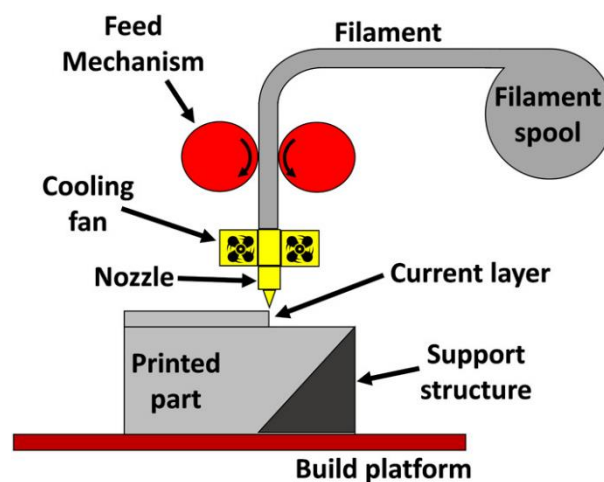


Figure 1.1. Schematic illustration of a typical FFF 3D printer [23].

The adhesion of the printed part to the build platform is also an important issue. There are various options for the build platform type, but mainly a glass surface is used [27]. The surface should be treated to enhance the adhesion between the part and the platform [28]. Also, as most filament materials need a heated build platform

to avoid detachment of the part from the platform due to warping [29], thus most of the printers are designed to have this feature by default.

There is no closed chamber in most cheap desktop 3D printers to create a controlled printing volume to control the ambient temperature. Even though there is some effort to reduce warping without a controlled atmosphere [27], the temperature-controlled printing chamber is necessary to avoid a failure due to warping during FFF printing with some thermoplastics, such as ABS [30].

However, most FFF 3D printers have a cooling fan to cool down the fabricated part, which is a need while printing most materials to enhance print quality, especially for printing parts with fine details [31]. Yet, it should be noted that printing a highly detailed part with a big build volume is not viable in FFF, as bigger nozzle sizes are needed to be used as the build volume increases, limiting the print resolution. Nozzle size also defines the print time. Therefore, nozzle size should be small enough to print the details with good resolution and big enough not to slow down the printing time [32].

Even though the surface roughness of the parts printed with FFF can be reduced by fine-tuning the process parameters [30], it is impossible to obtain a perfectly smooth surface. As the nozzle size and layer height are not negligibly small, the layers around the printed parts are generally visible, and the part should be treated if a smooth surface is needed [33,34]. However, some surface improvement methods, e.g., chemical treatment, may hinder the mechanical performance of the printed part [35].

The mechanical properties of the printed parts are strongly dependent on the printing parameters such as raster angle, printing temperature, layer height, and printing speed [23,36,37]. By tailoring these parameters, it is possible to print parts having mechanical strength comparable to the injection molded parts [38].

There are many FFF 3D printer types, which can be categorized according to print head placement, table and print head movement, and enclosure types.

1.2.1 Enclosure Types

FFF 3D printing is a scalable method; thus, it is possible to use it in a wide range, from cheap desktop printers to professional, factory-size printers. Most desktop printers do not have an enclosure to create a controlled ambient temperature during the printing, whereas professional FFF 3D printers mostly have an enclosure that provides a controlled cool-down period during the printing. Having an enclosure is an essential feature for printing materials sensitive to the cooling rate as they may exhibit significant shrinkage during cooling.

1.2.2 Extruder Placement Types

According to the position of the driving motor, there are two different extruder types, direct-drive and Bowden extruders [39].

In Bowden extruders, the driving motor is situated away from the hot end and print head assembly. Since the motor is not situated in the print head, the mass of the extruder carriage is lower compared to the direct-drive type. Thus, the inertia of the carriage is also lower, which allows more rapid and precise changes in tool path compared to direct drive during the printing, which increases the speed and accuracy of the FFF 3D printed parts.

However, the driving motor is close to the hot end in direct-drive extruders on the print head. Thus, it is much more convenient to print flexible materials in direct drive extruders, since in Bowden extruders, flexible filaments face buckling in the Bowden tube, which causes an increase of the friction forces, that may cause failure in printing [40].

1.2.3 Table and Printhead Movement

A relative motion should be created between the build plate and the nozzle to create a geometry in 3D. The table only moves vertically for most FFF printers, and the

printhead assembly moves in the horizontal axes. However, in some printers, the print head moves in the vertical and one of the horizontal axis, where the build plate moves in the other horizontal axis.

1.3 Multi-material FFF

Dual or multi extruder printers have become widely available recently. In the FFF method, one of the materials is usually used to produce the part, and the second material is the support structure material to support the overhanging parts, which can easily be removed after the printing is done [41].

Multi-material FFF printing also allows the printing of multiple structural materials within the same part. Thus, this approach offers an excellent opportunity to generate composite parts with unique mechanical behaviors designed to use for a deliberate function [42].

1.3.1 Single Nozzle

In single nozzle multi-material FFF printing, different material filaments are extruded using a single nozzle. Since there is only one nozzle, there is no need to calibrate each material [43]; however, purging needs to be done for material changing, and it is challenging for materials having different printing temperatures.

Nevertheless, by utilizing this method, parts having intermediate colors and color gradients can be printed by mixing different colored filaments in the hot end and extruding the molten thermoplastic from a single nozzle [44]. Therefore, it is also possible to blend compatible materials within the extruder to design and print a part with different mechanical properties in various locations.

1.3.2 Multiple Nozzle

Multiple nozzle multi-material printers have separate extruders for each filament; therefore, there is no need to replace filaments for printing multiple materials, reducing printing time [45].

There is no need to purge material after a filament change during printing; therefore, retraction of old and insertion of new filament, and purging time, thus material waste is averted. Each material has a separate hot end, making it possible to print materials with different print temperatures.

In multiple-nozzle printers, the distance between the nozzles should be carefully measured and given to the slicer as an input. Also, these systems require careful calibration, especially after the nozzle change, in the Z-direction. An uncalibrated inactive nozzle may harm the printed part, even may cause printing failure if the inactive nozzle height is lower than the active nozzle.

There are separate extruders in some multiple nozzle printers where their carriage can move along the rail to change the nozzle-to-nozzle distance. If more than one instance of an identical part is needed, printing them simultaneously is possible thanks to the extruders making the exact X-Y movement with a predefined offset.

1.3.3 Multi-Material Interfaces

Printing with multiple materials naturally introduces interfaces, which are one of the primary failure sites. The importance of the interfaces on the overall material strength becomes considerable when the materials are not alike, as the affinity of the materials is also a critical parameter for interface strength [46,47]. For these materials, the interfacial strength should be increased using mechanical bonding [48].

The strength of the interface also is dependent on the printing parameters such as nozzle and build plate temperature, print speed, and raster orientation [49,50]. As

Tamburrino et al. [51] founds, the printing order of the materials has an effect. Therefore, the printing parameters should be optimized to increase the interfacial mechanical strength.

1.3.3.1 Finite Element Modeling (FEM) of Interfaces

The finite element method (FEM) is a method to solve differential equations. In engineering, the FEM is used to differential equations that emerge from the solution of a physical problem, ranging from fluid mechanics, heat, and mass transfer to solid mechanics. Even though analytical solutions are available for simple geometries and boundary conditions, most real-life problems cannot be solved using analytical methods. By utilizing the FEM, complex geometries, boundary conditions, contact problems can be solved.

FEM is a tool used for finalizing the design details of a product and is sometimes used to understand the behavior of a part on certain load cases. FEM is also used to gather more information from an experiment since it allows to visualize the stress state of the part.

Cohesive Zone Modeling (CZM) is widely used to model the crack propagation in materials and is also used to modeling adhesive joints in FEM [52]. Utilizing this method makes it possible to define damage initiation and evolution parameters of these joints [53]. This method also allows the modeling of multi-material interfaces as it can be applied as a contact property between two different surfaces.

1.4 Materials Used in FFF

In the fused filament fabrication method, a spool of a filament of polymer thermoplastic material is used. Since the 3D printing enthusiasts mostly use the FFF method, the most widely used material is PLA since process parameters do not require rigorous tweaking to obtain strong parts. Since PLA is a biocompatible material, it is considered a safe-to-use material and even used to print toys for kids.

As shown in Figure 1.2., the market share of the TPU is minimal, with 2.5% compared to the PLA and ABS, having around 75% of the total market share of the filaments. One of the most critical parameters that lead to this excellent market share is the excellent availability and the low cost of these filaments. Also, most users select filaments that are easier to print and that have good reliability.

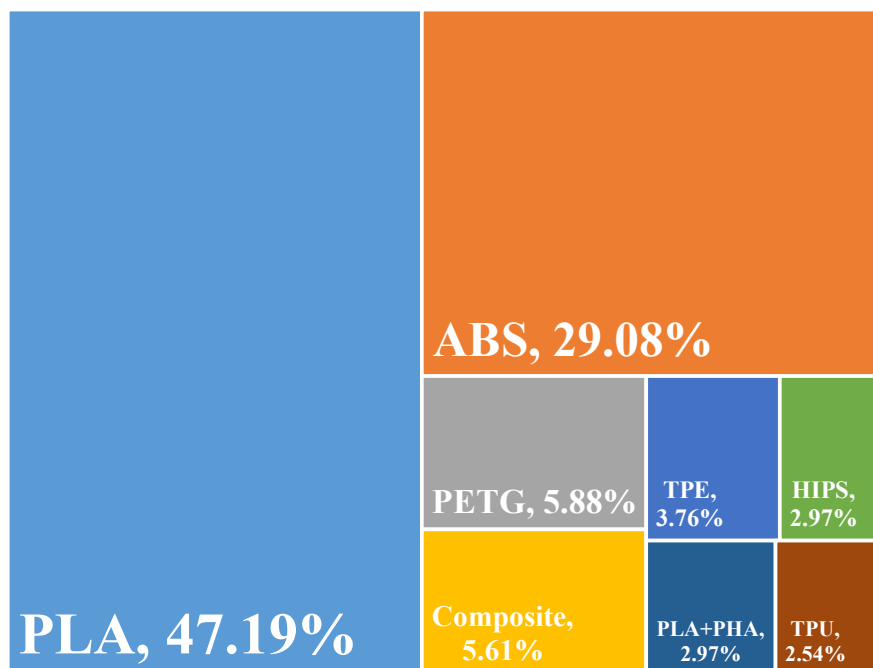


Figure 1.2. Market share of the FFF 3D printing filaments [54].

Several factors affect the quality of the FFF printed parts. First, even if the parts are produced through the FFF process designed with 100% infill, the density may change due to the under and over-extrusion, impacting the tensile strength of the printed part [55]. The storing conditions of the filaments are also should be taken care of as most of them are adversely affected by exposure to ultra-violet (UV) light [56] and high moisture environment [57]. The UV light breaks the bonds between the polymer chains, hindering mechanical performance [58]. As the moisture content of the filament increases, the printability of the filament decreases since (i), the excess

water content in the filament suddenly evaporates when heated up over 200°C, which is a typical printing temperature for most of the filaments, (ii) stringing occurs around the perimeter of the printed parts, especially the locations where the tools pass.

1.4.1 Acrylonitrile Butadiene Styrene (ABS)

Acrylonitrile Butadiene Styrene (ABS) is a widely used, low-cost material and exhibits good mechanical and thermal properties [59,60]. However, 3D printing of ABS using the FFF method is not a trivial task since the temperature of the print volume should be maintained at a required level to reduce the warping of the final product [30].

Also, the printing parameters should be selected carefully to optimize the mechanical performance of the part while printing with the ABS filaments since the process parameters have a profound effect [61].

1.4.2 Polylactic Acid (PLA)

Polylactic Acid (PLA) is a biodegradable material having good mechanical properties, thermal stability, and processibility [62]. PLA can be developed from 100% renewable resources [63]. Since it is a relatively cheap, eco-friendly, and easy to print material, it is the most widely used thermoplastic filament in FFF 3D printing [54].

PLA exhibits better mechanical properties compared to polypropylene (PP), polystyrene (PS), and polyethylene terephthalate (PET), while its thermal resistance is lower than theirs [62]. Even though the strength of the parts printed with PLA is relatively good, they exhibit low elongation at fracture, which can be increased with additions such as polyhydroxyalkanoate (PHA) [64].

It should be noted that similar to the other materials, the mechanical properties of the printed parts are affected by the raster orientation, moisture content, and color of the filament [65,66]. The printing conditions are also critical parameters as the cooling

rate affects the bond strength between layers and the print quality of the overall printed part [67].

As PLA is highly affected by the storage conditions, especially the relative humidity and UV light impact the ductility and strength of the printed parts, the storing conditions of the filaments and the use conditions of the printed parts should be optimal to increase the use time [68].

1.4.3 Thermoplastic Polyurethane (TPU)

While the initial use of FFF was limited to thermoplastics such as PLA and ABS, recent advances enabled the printing of elastomers with thermoplastic elastomer (TPE) filaments, which has excellent potential for FFF applications. Elastomers are rubber-like substances that exhibit large recoverable strains produced at low-stress levels [73]. One of the most widely used TPE is Thermoplastic Polyurethane (TPU), a copolymer consisting of hard and soft segments[69].

TPU is a flexible material with high toughness properties [70]. Thus, TPU is used in areas where flexibility and high toughness properties are needed. Even though it is not a biodegradable material [71], Xiao et al. [72] produced medical-grade biocompatible TPU filament.

1.4.4 Polyamide (PA)

Polyamide (PA), known as nylon, has been utilized in the industry for almost a century. A naming system is used to describe different synthetic PA structures, such as Nylon-6, Nylon-12, Nylon-6,12, where nylon in the naming can be changed with PA. Being commonly used in biomedical applications, PA is a biocompatible material exhibiting good mechanical properties with high chemical stability [74]. PA is a material that can play a crucial role in the aerospace industry due to its good flexural and fatigue strength while being a low-density material (1g/cm³) [75]. However, one of the most significant drawbacks of the FFF printed PA-6 is the

warping [76]. The warping problem could be overcome by using an adherent between the build plate and the printed part and printing in a controlled temperature environment.

1.4.5 Carbon Fiber Reinforced Polymers

Carbon fibers (CF) are added to the polymer filament matrix to improve the printed parts' overall mechanical, thermal, and chemical properties [77]. The primary intention is to improve these properties, so the amount and the CF type should be tailored. When the weight percent of the CF addition increases, some of the mechanical properties may show a decline [78,79].

These additions have three main groups: carbon nanotube (CNT), continuous CF, and cropped CF.

1.4.5.1 Carbon Nanotube (CNT) Additions

Carbon nanotubes (CNTs) are orders of magnitude smaller particles than the commercial filament diameter and length; thus, they disperse in the polymer matrix uniformly [80]. Therefore, carbon nanotube addition to a polymer matrix increases the mechanical properties, regardless of the raster orientation [81].

1.4.5.2 Continuous CF Additions

Continuous CF addition is achieved by inserting the fiber via an opening to the extrusion head to the hot end where thermoplastic material is melted [82].

Heidari-Rarani et al. [83] and Li et al. [84] found that continuous CF addition to the PLA increases the tensile strength up to 35% and bending strength more than twice, compared to the pure material, which shows that the continuous CF composite has an excellent potential for manufacturing lightweight, robust and complex parts which

makes them a desirable material, especially for the aerospace industry. Still, printing with continuous CF is a complicated task, as it is needed to print in a continuous path, which might be impossible for printing some parts; therefore, a redesign might be needed.

1.4.5.3 Chopped CF Additions

The chopped CF additions are in between the CNT and continuous CF additions. The literature shows that the length of the chopped CF addition is on the order of $100\mu\text{m}$ [77,78,85,86]. Even if the CF length before the process is in the order of millimeters, the average length drops around tenfold during the mixing phase of CF and polymer [87].

Chopped CF addition into a polymer matrix can improve the mechanical performance of the printed carbon fiber reinforced plastics (CFRP), especially tensile strength and Young's modulus; however, it should be noted that toughness, yield strength, and ductility may decrease [78].

As Brenken et al. [88] summarized, the raster angle of the printed specimens affects the tensile modulus in such that the tensile modulus of 0° raster angle specimens is higher than the 90° raster angle specimens. It is also found that CFRP that has chopped CF as reinforcing material is influenced by the raster angle more profoundly than the CFRP with CNT. Zhang et al. [81] observed that at a 90° raster angle, the tensile strength of the CF added ABS CFRP is lower than the pure ABS while the tensile modulus does not change considerably. They also found that, at 0° raster angle, the tensile modulus of the CF added ABS almost triples the pure ABS, whereas CNT added ABS does not differ from the pure polymer.

1.5 Infill Patterns Used in FFF

It is often needed to strengthen the 3D printed structure with an infill geometry as parts are mostly printed as a shell structure having internal cavities and overhanging regions. The shape of infill geometry affects the overall strength of the printed part and enables the design of parts exhibiting unique stress-strain relationships.

The most widely used infill type is the rectilinear infill due to its great applicability for various printed part sizes and shapes. The rectilinear infill is constructed only by straight lines, so programming effort is less compared to the more complicated infill patterns.

Even though a simple rectilinear or grid infill was one of the few choices in FFF in the initial stages, most of the slicing software added a variety of infill types to give users more opportunity to select an infill type according to the material, printing, and use conditions of the printed parts. Each slicing software offers different infill patterns, but the basic infill patterns are available almost in all of them. The commonly used infill types are rectilinear, honeycomb, triangular infills. Moreover, it is possible to design in-house infill types, which enables users to fine-tune the mechanical and thermal properties of the printed part.

1.6 Thesis Work

This thesis investigates the mechanical characterization of the interface of 3D printed PLA-TPU multi-material produced by FFF. The findings will extend the knowledge about the interfaces of the 3D-printed materials and facilitate their use in industrial applications.

It is possible to obtain unique material behavior by combining the stiff and compliant phases in the same structure. Mechanical properties of these FFF 3D-printed multi-material parts have not been characterized in detail. The interface characteristics and ways to improve the interfacial strength are not well known.

Even though the CF reinforced thermoplastic filaments are thoroughly investigated in the literature, the infill geometry's effect on compressive loads on parts printed with CF reinforced filaments is not well-studied. By altering the infill geometry, it is possible to tune the strength and toughness of a part.

In this thesis, I concentrated on composite structures produced through the fused filament fabrication method. The first focus of the thesis will be multi-material printing. I investigated the mechanical properties of multi-material 3D-printed objects' interfaces, explored ways to enhance their performance. The second focus is the mechanical characterization of the commercial PA and CF reinforced PA filaments. In this part, the mechanical properties of parts printed via the FFF method with different infill patterns are characterized through tensile and compressive tests.

CHAPTER 2

ELASTOMER-PLA INTERFACES PRODUCED BY FFF

2.1 Introduction

Until the recent decade, only one material could be printed using the FFF method since the unavailability of multi-material 3D printers. However, as multi-material printing has become accessible in the last decade, printing parts with multiple materials or colors is possible.

Understanding the interface behavior and assessing strength is an essential task for multi-material printing as the interfaces are one of the main fracture sites. Thus, it is vital to pinpoint that whether mechanical bonding is needed or not. It is also important to evaluate the effect of mechanical bonding for optimizing the interface geometry as more involved interface geometries are trickier to print and increase the printing time.

PLA is the most widely used polymer filament and exhibits plastic behavior, whereas TPU is a widely used polymer filament showing elastomeric behavior. These are dissimilar materials, and their interfacial strength is relatively low. Therefore, these filament materials were selected to evaluate the effect of mechanical bonding between them and also due to the availability of these filament materials.

2.2 Experimental Details

In this work, the interface properties of PLA (Ultrafuse PLA Blue – 1.75 mm, BASF, Germany) and TPU (Ultrafuse TPU 85A – 1.75mm, BASF, Germany) materials were investigated. This part involving in designing, printing, and mechanical testing of custom dogbone specimens. First, PLA and TPU specimens were printed to

understand the mechanical behavior of these materials. Then, multi-material dogbone specimens were designed to understand the interface behavior and evaluate the interfacial strength along the normal and the shear directions. Finally, specimens having comb-like interface geometry were printed to understand the effect of the mechanical bonding and comb length on the overall strength.

2.2.1 Sample Geometries

To assess the mechanical properties of PLA, ASTM D638-14 Type IV specimens were printed, and uniaxial tensile tests were conducted [89]. For the TPU, a half-scaled version of the ASTM D638-14 Type IV specimen was printed.

The technical drawing of the PLA and TPU specimens are given in Figure 2.1. Two different sets of specimens were printed to understand the interfacial tensile strength and shear strength. The specimen geometry in Figure 2.1 (d) was printed with an x value of 0, which creates a flat interface to assess the interfacial strength in the normal direction. A shear test specimen was designed for measuring the shear strength, and the technical drawing of the part is given in Figure 2.1 (c).

Technical drawing of comb-like specimens is shown in Figure 2.1 (d). Specimens having three different comb lengths (2, 4, and 6mm) were investigated. PLA and TPU specimens were named using abbreviations P and T throughout the project, and multi-material parts were named differently. The multi-material specimens were specified using a convention as TPx , where T stands for TPU, P stands for PLA, and x designates the length of the interface. For instance, the flat interfaced specimen is TP0 since the comb length is zero millimeters, and specimens with a 6mm comb length are named TP6. While designing the specimens in Figure 2.1 (c) and (d), the dimensions of standard specimens were used as much as possible. However, to enhance the effect of the interface, the width of the narrow section was increased. It was also done to print combed specimens with more comb numbers with adequate print quality at the comb regions since a 0.4 mm nozzle was used while printing.

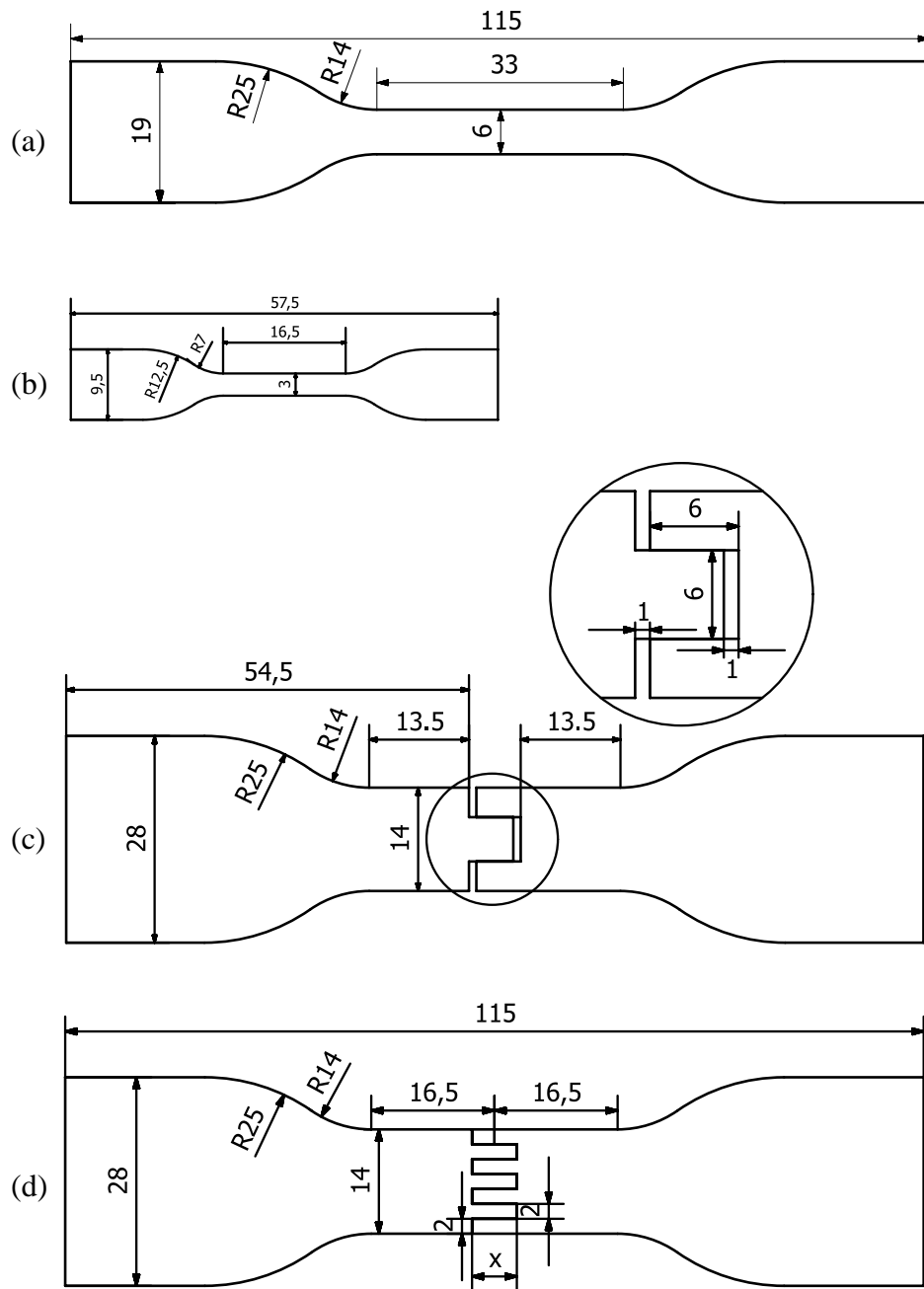


Figure 2.1. Tensile test specimens (a) PLA (b) TPU (c) Shear Test (d) Combed. Comb length is given as "x" in the drawing, which was used as 0, 2, 4, and 6 mm in this project. The thickness of (a), (c), and (d) is 3.2mm, and (b) is 1.6 mm.

2.2.2 Sample Preparation

All samples were 3D printed using the FFF method, and they were prepared in three main steps, which are 3D CAD modeling, generating toolpaths, and printing.

2.2.2.1 3D CAD Modeling and Toolpath Creation

The first step of preparing a 3D printed sample is the 3D CAD modeling, then a machine code that contains the toolpath is created. The machine code is needed as the FFF 3D printing operation is an automated process.

It is not possible to directly 3D print by using the 3D CAD model of a part. A slicer software needs to be used to generate toolpaths using a 3D CAD model used in the 3D printer. Therefore, after completing the drawing of a part, an STL model is exported to use in slicer software to generate toolpaths.

Throughout this part of the thesis work, Siemens NX 11.0 (Siemens, Germany) was used to draw the 3D CAD model of the specimens, and Simplify3D (Simplify3D, Cincinnati, Ohio – USA) slicing software was used to generate toolpaths. The STL files were imported to the Simplify3D, and the corresponding printing parameters were applied. The toolpaths were exported to X3G format to be able to use in the printer.

2.2.2.2 3D Printing

A FlashForge Creator Pro (Zhejiang Flashforge 3D Technology Co., Ltd, China) FFF dual extruder open-source 3D printer, shown in Figure 2.2, was used to print all PLA, TPU, and multi-material parts. The printer has a top cover; thus, printing in a fully enclosed environment is possible. However, as neither PLA nor TPU does not require ambient temperature control, the cover was not used. The printer has a direct-drive extruder setup, which makes it convenient to print flexible TPU filament.

In the stock conditions of the printer, the printing platform has a heater, which can go up to 120°C, and a 6 mm thick aluminum plate is placed over the heating element, which helps to heat the build plate evenly. A rough printing surface was glued on the aluminum plate to enhance the adhesion between the parts and the printing platform.

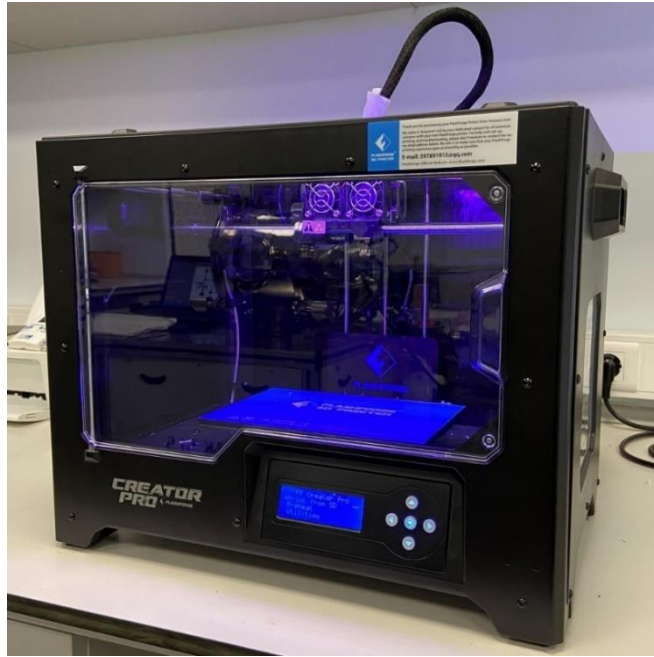


Figure 2.2. Flashforge Creator Pro dual nozzle FFF 3D printer.

The printing parameters are given in Table 2.1. The printing parameters were selected using the filament manufacturer's directions as a guide and finalized through printing PLA and TPU parts with different settings. The bed temperature was selected as an intermediate value to increase the adhesion of both PLA and TPU to the printing platform. The parts were printed using only one shell to decrease the influence of the wall structure while maintaining the outer surface quality. Furthermore, to minimize anisotropic behavior that may result from the infill directions, the parts were printed with a 100% infill with a $\pm 45^\circ$ raster angle.

Table 2.1. FFF 3D printing parameters for PLA, TPU, and interface specimens.

Parameter	
Filament Diameter	1.75 mm
Nozzle Diameter	0.4 mm
Layer Thickness	0.2 mm
Printing Speed (PLA, TPU)	40, 15 mm/s
Nozzle Temperature (PLA, TPU)	210, 220 °C
Bed Temperature	40 °C
Number of Shells	1
Infill Directions	$\pm 45^\circ$

3D printed PLA and TPU tensile test specimens are given in Figure 2.3. For each material, three specimens were printed for uniaxial tensile tests. The specimens were printed one by one to optimize the toolpath so that the printhead does not cross over the previously printed sections. Each specimen is printed at the same location on the build plate to increase repeatability.



Figure 2.3. 3D printed PLA and TPU dogbone specimens. (i) PLA specimen was printed using Ultrafuse blue PLA filament, and the (ii) TPU specimen was printed using Ultrafuse TPU 85A filament. The *P* in the naming indicates that the material is PLA, and *T* indicates that the material is TPU.

The photographs of 3D-printed multi-material parts having a flat interface (i), shear test specimen (ii), and comb interface specimens having comb lengths of 2, 4, and 6 mm (iii to v) are given in Figure 2.4.

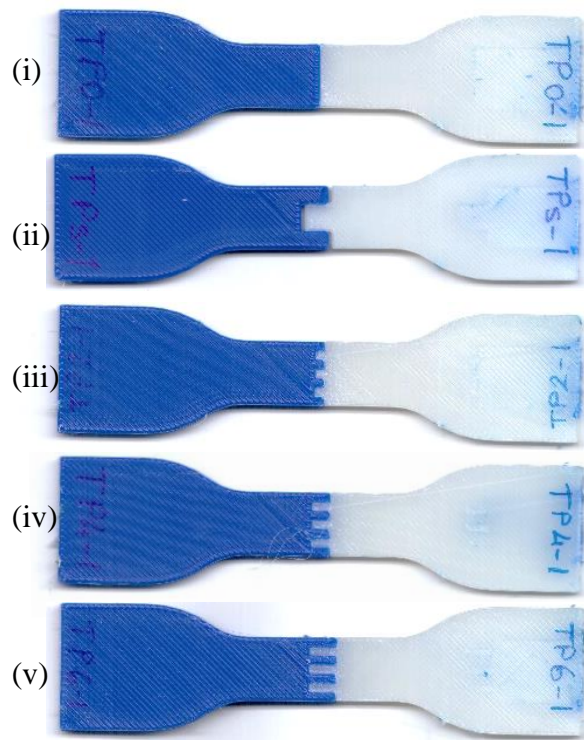


Figure 2.4. Flat interface specimen (TP0) (i), shear test specimen (ii), and combed specimens having (iii) 2 mm (iv) 4 mm (v) 6 mm comb lengths. Blue parts are printed with PLA and white parts with TPU filament.

2.2.3 Mechanical Testing

The uniaxial tensile test is a versatile method to evaluate mechanical material properties as it gives a handful of data with a single test. Since the test is well known and has various international standards, it is good to conduct a uniaxial tensile test to assess material properties as it is possible to compare with the available data in the literature. By performing a uniaxial tensile test, elastic modulus, yield strength,

ultimate tensile strength, elongation at break, and toughness of a material can be evaluated.

Uniaxial tensile tests were conducted using a uniaxial material testing machine (Z250, Zwick/Roell, Germany) at room temperature. The cross-head speed was selected as 5 mm/min for the PLA, which complies with the ASTM D638-14 standard [89], while the test speed for the TPU specimen was selected using the ASTM D412-16 standard [90], as 500 mm/min.

Since there were materials with different mechanical properties in the multi-material test specimens, the test speed needed to be selected to satisfy the test conditions of each material as much as possible. The test speed was selected to be 500 mm/min, as the UTS of the TPU is much lower than the PLA, and the failure of the multi-material test specimens was predicted to be at the interface, i.e., not the failure of the constituting materials. As the gauge length of the combed specimen doubles the gauge length of the TPU specimen, and exactly half of the combed specimen was printed with the TPU, the length of the narrow region of the TPU is the same; thus, the strain rate along the test direction remains the same.

The tensile stress, σ_T , for TPU and PLA specimens was calculated using equation (1), simply dividing the tensile force, F_T , by the cross-sectional area of the narrow region, A_T , of the dogbone specimen.

$$\sigma_T = \frac{F_T}{A_C} \quad (1)$$

For assessing the mechanical performance of the combed specimens, effective stress, σ_E , is calculated in a similar fashion to the single-phase materials, using equation (2). The effective stress is calculated by dividing the tensile force by the initial cross-sectional area of the narrow region of combed specimens. By calculating the

effective stress value, it is possible to compare specimens having different comb lengths.

$$\sigma_E = \frac{F_T}{A_C} \quad (2)$$

The shear strength of the shear test specimens is calculated using equation (3), where σ_{shear} is the shear stress, A_{shear} is the shearing area. As there are two shearing surfaces in the test specimen, both interface areas were considered.

$$\sigma_{shear} = \frac{F_T}{A_{shear}} \quad (3)$$

The tensile stress occurring in TPU in the comb region, $\sigma_{comb,TPU}$, can be calculated using equation (4).

$$\sigma_{comb,TPU} = \frac{F_T}{A_{comb,TPU}} \quad (4)$$

Where, $A_{comb,TPU}$ is the cross-sectional area of the TPU in the comb region.

2.2.4 Finite Element Modeling

Computer simulations were performed to gain more insight into the experiments. For computer simulations, Abaqus 2021 Finite Element Software (Dassault Systèmes, France) was used as a solver and pre-post processor on an HP Z240 Workstation (HP Development Company, L.P., USA).

The main goal of the simulations in this work was to mimic the experiments to gain more insight from the experiments, for example, the stress state at the interface region. To achieve this, the exact 3D CAD models that were used to print the specimens were used. Also, for tensile test simulations, the clamped regions of the dogbone specimens were selected for enforcing displacement boundary conditions. Half and symmetrical quarter models were used when applicable to decrease computational effort.

The standard Abaqus interface was used as a pre and post-processor. The solid bodies were partitioned, and both global and local mesh seeding is done to increase the accuracy of the simulation by fine-tuning the mesh size and increase mesh quality. Mesh independence studies were done for each case, and the coarser mesh size that gives adequate results were selected to minimize the simulation time while identifying the material and contact parameters.

Firstly, a tensile test of a PLA specimen was simulated with the material properties obtained from the mechanical tests. For modeling the material, the default elastic-plastic material model of the Abaqus was used. Then a tensile test of a TPU specimen was simulated using a hyperelastic material model. The tensile test data was used to fit hyperelastic material models in the software, and the best-fitted model was selected.

For modeling tensile tests of the PLA and TPU specimens, the quarter model of the dogbone specimens was used with appropriate symmetry boundary conditions. The corresponding geometry and the boundary conditions are shown in Figure 2.5. After the simulations were done, the displacement information was obtained from the node situated at the location of the extensometer that was used in the mechanical tests. The loading boundary conditions were applied to the surface where the jaw of the tensile test machine holds and pulls the specimen.

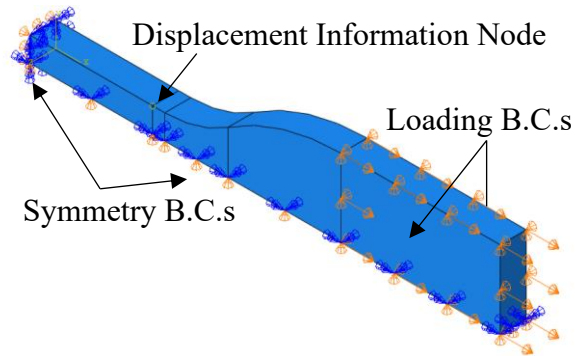


Figure 2.5. The screenshot showing the boundary conditions used in the simulations of PLA and TPU specimens.

The PLA specimen was discretized with 531 linear hexahedral elements of type C3D8R, and the total number of nodes was 960, whereas the TPU was discretized with 1460 linear hexahedral elements of type C3D8RH, and the total number of nodes was 2220.

The multi-material parts were modeled using the material properties verified in the previous step. For modeling the interfaces of the multi-material parts, cohesive zone modeling (CZM) was utilized through surface contact interactions. The interface strength was found by changing the tensile and shear strength values for each simulation. A screenshot of discretized TPO specimen is given in Figure 2.6, where the total number of nodes is 14820, the total number of elements is 11088, composed of 5544 linear hexahedral elements of type C3D8R, and 5544 linear hexahedral elements of type C3D8RH.

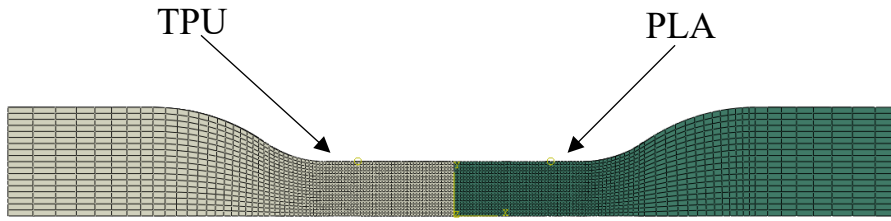


Figure 2.6. Screenshot of discretized flat interface specimen, half of the specimen was modeled using symmetry boundary conditions.

A screenshot of the discretized tensile shear test specimen is given in Figure 2.7. The total number of nodes was 29307, and the total number of elements was 24270, composed of 9870 linear hexahedral elements of type C3D8R and 14400 linear hexahedral elements of type C3D8RH. The symmetry boundary conditions were not used while modeling the shear tensile shear test specimen as the fracture of the specimen did not occur symmetrically during the experiments. The interface regions were modeled using the CZM.

Due to the nature of the FFF process, there is always sub-millimeter level miscalibration in both X and Y axes. Therefore, it was impossible to use the results obtained from the simulations of the flat interface specimen directly; thus, the stiffness, tensile, and shear strength parameters of the shear test specimen were found by changing them one by one and obtaining simulation results. Different damage initiation parameters were used for each contact interaction to evaluate the interface strength of each interface.

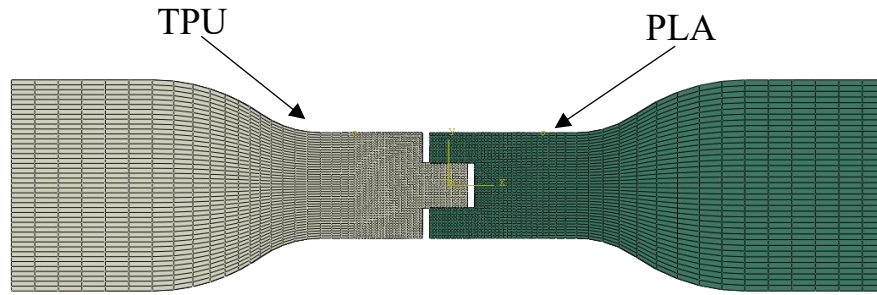


Figure 2.7. Screenshot of the discretized tensile shear test specimen, half of the specimen is modeled using symmetry boundary conditions.

2.3 Results and Discussion

2.3.1 Experimental Results

After the uniaxial tensile tests, photographs of the fractured PLA specimens were taken, and one of the specimens is given in Figure 2.8. When the fractured region was investigated, it was seen that the fracture occurred abruptly, without showing signs of ductility. Therefore, by only observing the fracture photography, it can be said that the toughness of the material is poor. The elongation at the break value of the PLA was found around 2%, which is a low value in terms of ductility.



Figure 2.8. Fractured PLA tensile test specimen after the uniaxial tensile test.

The high ductility of the TPU specimens was seen clearly in the fractured photo of the tensile test specimen given in Figure 2.9. TPU specimens were extended over six

times compared to their original length. Plastic deformation that occurred in the material was observable through the discoloration such that the color was turned to white in the regions where permanent deformation occurs.



Figure 2.9. Fractured TPU tensile test specimen after the uniaxial tensile test.

The photograph of a flat interface and shear test specimens taken after the tensile test is given in Figure 2.10 (i) and (ii), which shows that the fracture occurred only in the interface, and there is no visible permanent deformation neither in PLA nor TPU parts. Since there is no discoloration in the TPU, it can be deduced that there was no gross plastic deformation.

In Figure 2.10 (iii) to (v), the photographs of fractured combed specimens after the tensile tests are given. There is no visible permanent deformation in either specimen when the comb length is 2 mm and 4 mm. However, in the case (v), when the comb length is 6mm, there is a visible permanent deformation seen as whitening in the root of the comb region of the TPU specimen.

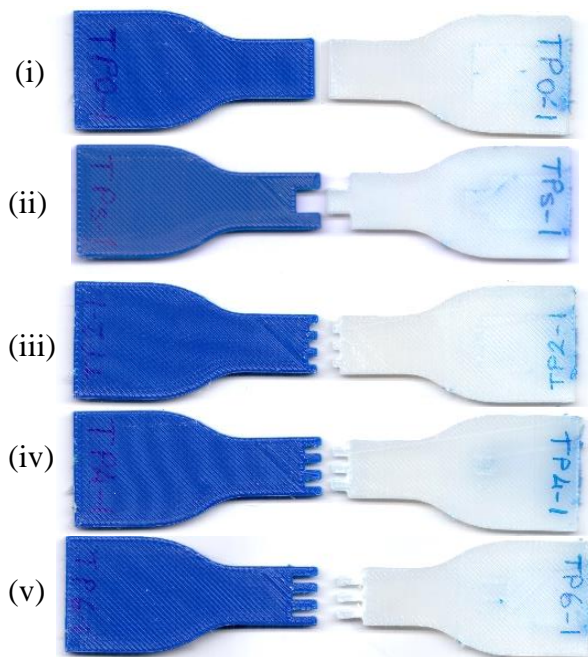


Figure 2.10. The photographs of multi-material specimens after the uniaxial tensile tests. The flat interface (i), shear test specimen (ii), and combed specimens having (iii) 2 mm (iv) 4 mm (v) 6 mm comb lengths.

The difference in the tensile test results in terms of the mechanical properties of the PLA and TPU can be further observed in Figure 2.11. When a comb having 2 mm length was introduced, the UTS of the overall part rapidly increased. Increasing the comb length to 4 mm enhanced the strength of the TP4 specimen better compared to TP2.

However, when the comb length further increased to 6 mm, the UTS value decreased slightly, which illustrates that there is a sweet spot for comb length to increase the overall part strength. Therefore, while designing a multi-material part composed of PLA and TPU, the comb length should be selected carefully to decrease the intrusion length if the goal is to increase the interface strength, as the overall print time increases as the comb length increases.

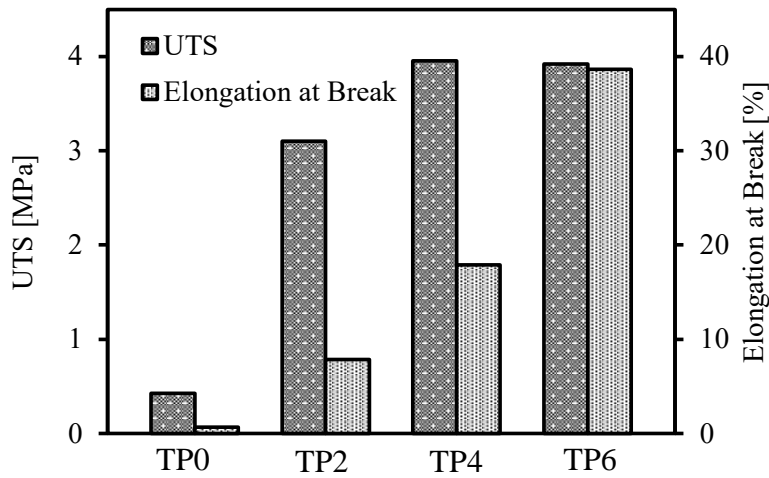


Figure 2.11. Tensile test results of TPU-PLA multi-material interface specimens.

The elongation at break data of the comb-like specimens is given in Figure 2.12. as a bar chart. In TP0 specimens, the maximum elongation was minimal, well below a millimeter. As there were no mechanical enhancements, this specimen primarily exhibited the tensile strength of the interface. The low interface strength in TP0 specimens was a sign that the affinity of the TPU and PLA was relatively low, and mechanical improvement was needed in the interface to improve interfacial mechanical strength.

When the comb length is 2mm, the elongation at break was almost the same as the comb length; therefore, there was a remarkable improvement with the introduction of a comb-shaped intrusion even though the shape was along the tensile test axis.

The comb shape not only increased the effective interfacial area but also introduced a new interface failure mode, the shear failure of the interface. Since there were six shearing faces in the comb interface specimens, the shearing length, in this case, is 12 mm, whereas the length subjected to tensile stress remains 14mm. Even though the introduced shearing area was less than the tensile area, its effect on the overall performance of the test specimen was remarkable.

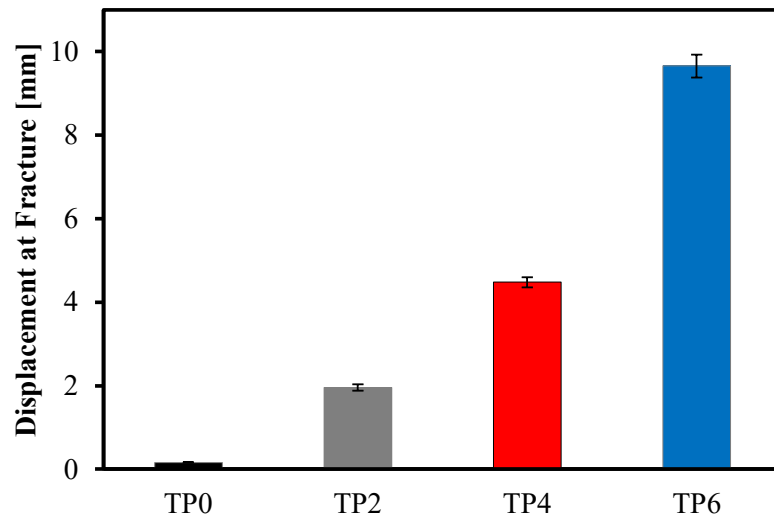


Figure 2.12. Displacement at fracture of the comb interface specimens having 0, 2, 4, and 6 mm comb lengths.

When the tensile test results provided in Figure 2.13 are investigated, it was seen that, compared to the overall strength increased due to the addition of the shearing areas, the tensile strength of the interface was almost negligible.

As the comb length was further increased to 4mm, the elongation at the break value went beyond the comb length of the specimen. Therefore, an additional 2 mm was more effective compared to the initially created 2 mm inclusion. Moreover, there was a plateau region in the stress-strain graph which maintained almost the same stress level from 5% strain to the fracture of the specimen.

Further increasing the comb length improved the elongation at break value much more efficiently than 2 and 4 mm comb lengths. In these cases, the added extension value was around 2 mm; however, in the 6 mm comb length specimen, the marginal elongation at break value was over 4mm. Thus, the test results reveal that, as the length of the comb increase, the effectiveness of the combs improves.

The effect of the comb length on the elongation at break value is also evident in the effective stress versus tensile deformation graph in Figure 2.13. Remarkably, the plateau stress is almost the same for 4 and 6mm comb length specimens, which is around 4 MPa. Since the elongation has occurred primarily in the TPU, it can be said that the plateau stress is related to the stress state of the TPU specimen.

When the stress-strain curve of the TPU given in the inset (ii) in Figure 2.13 is examined, it is seen that there is a plateau region below 10 MPa. To compare this value with TPU in the combed specimens, the cross-sectional area of the TPU in the comb region should be taken into consideration to assess the stress value in this region, which is calculated using equation (4). The results show that the plateau stress of TPU in the comb region is around 9 MPa.

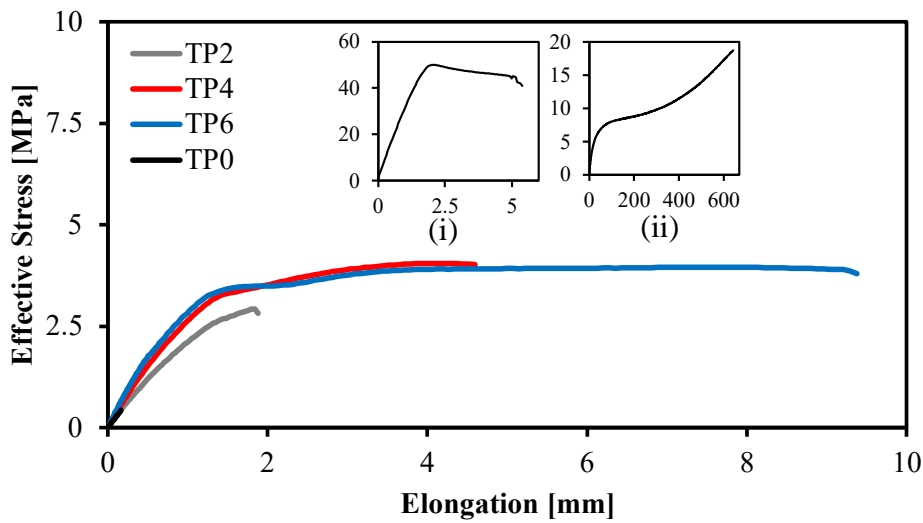


Figure 2.13. Effective stress versus tensile deformation response of the combed specimens having 0, 2, 4, and 6 mm comb lengths. The insets are (i) stress versus percent elongation graph of the PLA tensile test specimen and (ii) stress versus percent elongation graph of the TPU specimen.

The shearing stress versus elongation graph of shear test specimens is given in Figure 2.14, where the shear stress is calculated using equation (3), and the elongation value shows the tensile elongation of the shear test specimen in the gage length.

When the curves are investigated, it is seen that there is a linear elastic region up to around 1 mm of elongation. Then, a plateau-like region is followed by another linear region with a lower tensile modulus value compared to the first elastic region. The first and second tensile modulus of the three shear test specimens were almost the same; however, the length and the stress value of the plateau regions were different.

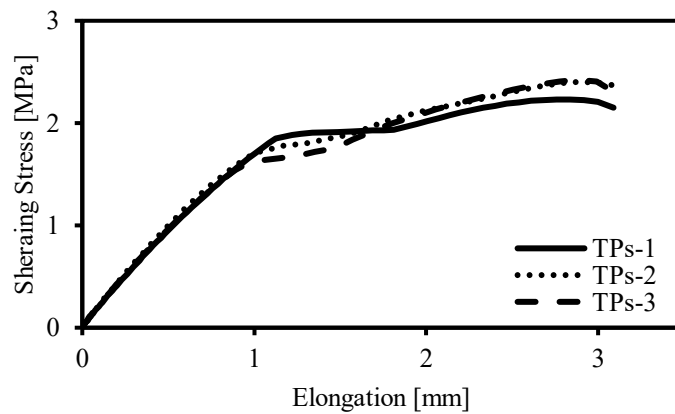


Figure 2.14. Stress versus elongation diagram of the shear stress test specimens. Shearing stress is calculated using the total interfacial area. The elongation value shows the total tensile elongation of the tensile test specimen in the gage length.

To better understand the mechanical behavior of the shear stress test specimens, a high-speed video was captured during a tensile test, and pictures taken from the video are given in Figure 2.15. When these pictures are investigated, it is seen that the fracture does not occur symmetrically with respect to the tensile test axis. This behavior probably was originated from the minor calibration problem that cannot be

fixed fully in the FFF 3D printer that creates a positive air gap at the right and a negative air gap at the left interface region.

The sudden failure of the interface at the right caused the creation of the plateau region in the stress-strain diagram. As the interface at the right side breaks before the left side, the overall tensile modulus of the test specimen decreases due to a reduction in effective load-bearing area, which explains the decline in the tensile modulus after the plateau region.

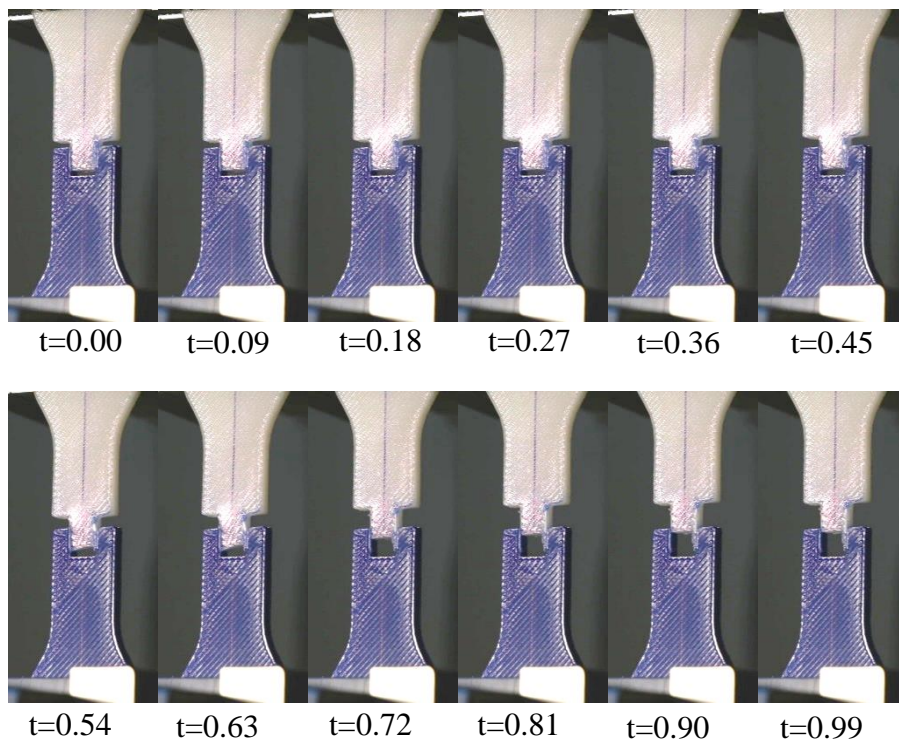


Figure 2.15. The snippets from the tensile test video of the multi-material shear tensile test specimen. The blue markings are drawn with a pen for alignment and to use in the post-processing of the video.

The pictures of the high-speed video of the tensile test on a specimen having a 6 mm comb length are given in Figure 2.16. Due to increased interface strength, a visible

fracture does not occur until 0.7 seconds, then a rapid lengthening is observed in the comb region. The first failure is seen in the root of the comb region of the TPU part. Then, the combs continue to lengthen until 0.9 seconds, then a sudden failure occurs. Although the combs are extended to almost doubling their original length, they went back to their original length after the fracture. Also, there is no visible deformation in the comb region of PLA.

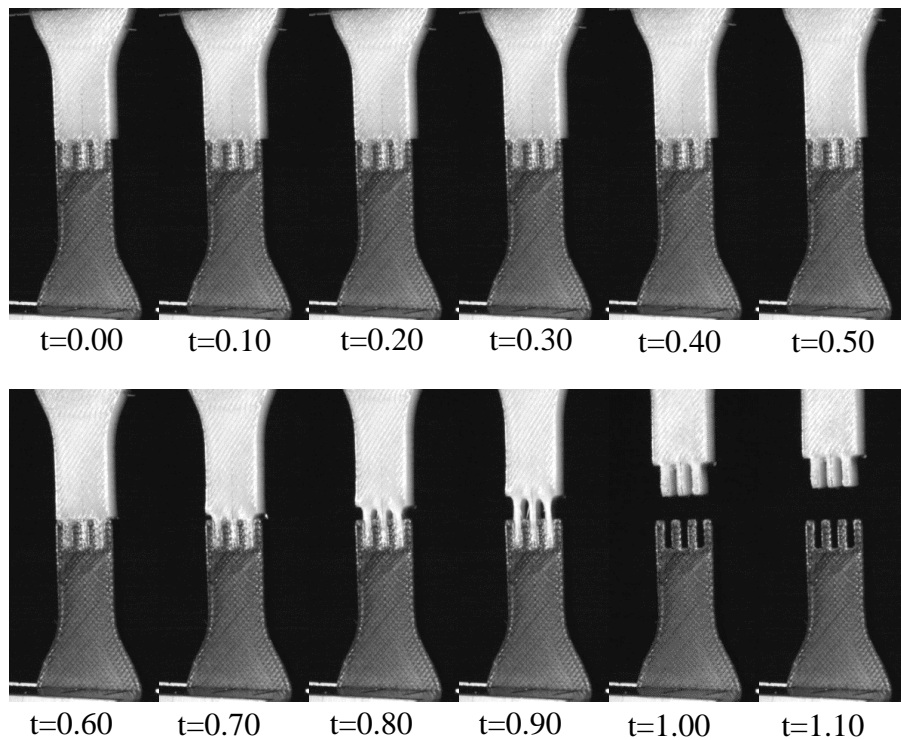


Figure 2.16. The snapshots from the tensile test video of the multi-material combed tensile test specimen with a comb length of 6 mm.

An optical microscopy image was taken from the TPU part of the fractured tensile shear test specimen, as shown in Figure 2.17. The fracture surface is not smooth; there are wedge-like intrusions and extrusions along the surface, with a 100 μm length on average. This irregular geometry acts as a mechanical bonding pattern;

therefore, it can be deduced that FFF 3D printed multi-material parts have a mechanical bonding inherently due to the nature of the printing process.

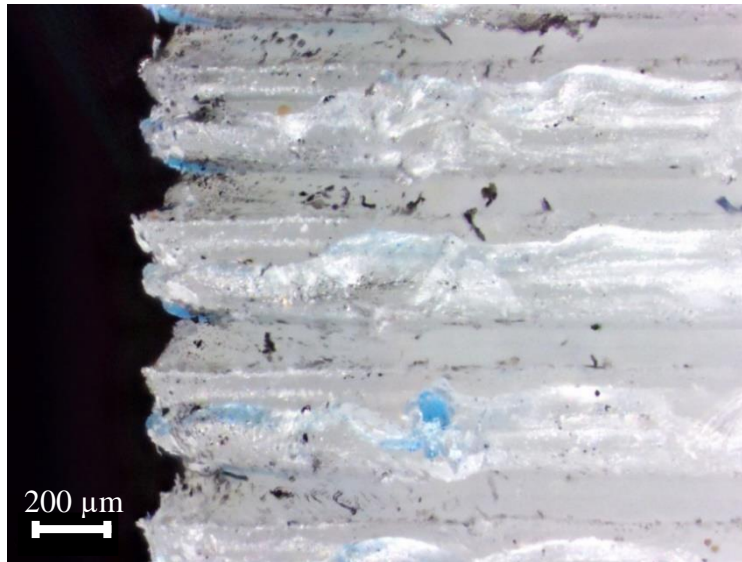


Figure 2.17. Optical microscopy image of a fractured interface of TPU part of the dogbone tensile shear test specimen.

However, it should be noted that due to misalignments in the X and Y axes, as mentioned before, this wavy structure does not have the same geometry and length in all directions. Therefore, the mechanical bonding achieved only with the wavy interface does not give a uniform bonding strength, and interlocking patterns should be incorporated to obtain a more reliable interface.

2.3.2 FEM Results

A comparison of the experimental results and FEM analysis of the PLA and TPU specimen is given in Figure 2.18 (i). As the elastic modulus of the value of the PLA is measured from the initial elastic region and set to 3200 MPa, and the yield strength is selected to be equal to the UTS. The plastic deformation is modeled using the

available tensile test data. There is a slight difference between the 1 and 2% strain range. After the yielding, the simulation result shows a good agreement with the tensile test.

On the other hand, the simulation result of the TPU specimen almost perfectly coincides with the tensile test result, as can be seen in Figure 2.18 (b). The selected material model for TPU was the Ogden, which was the model that gave the best matching results in the Abaqus software.

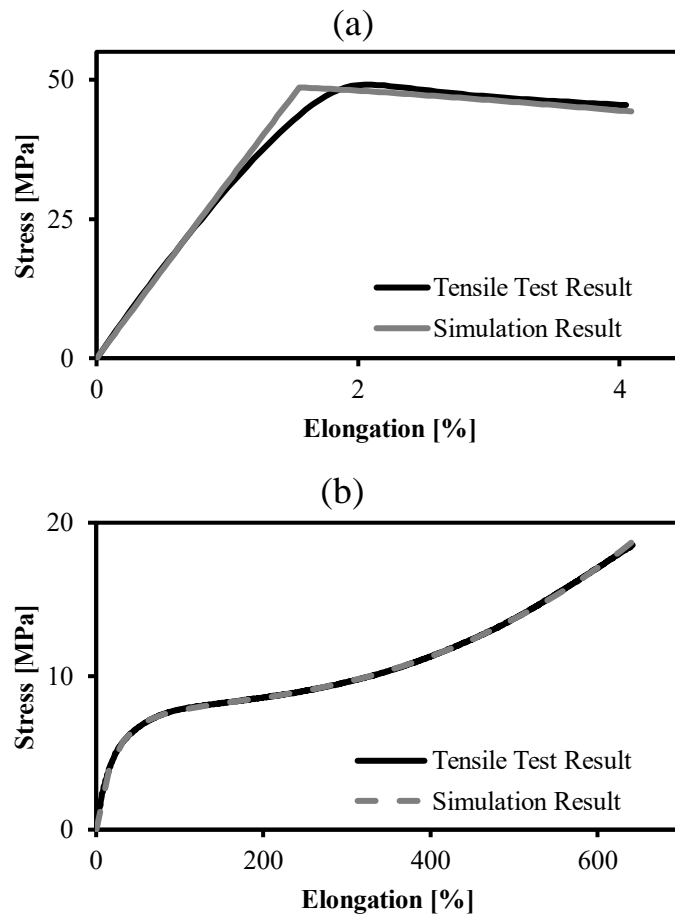


Figure 2.18. The tensile test result versus simulation result graph for (a) PLA and (b) TPU specimens.

It should be noted that, even though the Ogden model predicted the stress-strain behavior of the specimen remarkably good, it is possible to obtain the same behavior with different coefficients in the model when only the uniaxial tensile test is used for fitting, which may lead to erroneous results [91,92]. The Ogden model was used as the simulation results of other models gave inaccurate stress-strain behavior compared to tensile test experiments, and the results obtained with the Ogden model were accurate.

In multi-material specimens, most of the tensile deformation occurs in the TPU part. Also, there was no observed gross plastic deformation in the PLA; therefore, the UTS value of the PLA was not exceeded. Therefore, it was deduced that the material models obtained in the previous step could be used for modeling the multi-material specimens.

While modeling the interface specimens, the materials are modeled with the PLA and TPU material properties found in the previous step. Contact interactions were used for modeling the interface of PLA and TPU. The Cohesive Zone Modeling (CZM) was used since it is possible to control the damage initiation and propagation properties with this model. The damage initiation and evolution values are iteratively found for flat interface and shear test specimens.

However, assessing the damage initiation and evolution parameters was not a trivial task. Even though the tensile strength of the interface seems to be 0.4 MPa, as found in the tensile test, inserting as a damage initiation value caused erroneous results. The error stems from the fact that the fracture at the interface does not occur abruptly; instead, there were crack initiation and propagation phases.

The stress state of the flat interface specimen, taken just before the crack initiation, is given in Figure 2.19 (a). The stress state is not uniform in the vicinity of the interface for both TPU and PLA, and the maximum stress occurs at the corners for both specimens. Therefore, crack initiates from the corners of upper and lower edges

simultaneously, as seen in the second snippet is shown in Figure 2.19 (b), then propagates to the center of the interface.

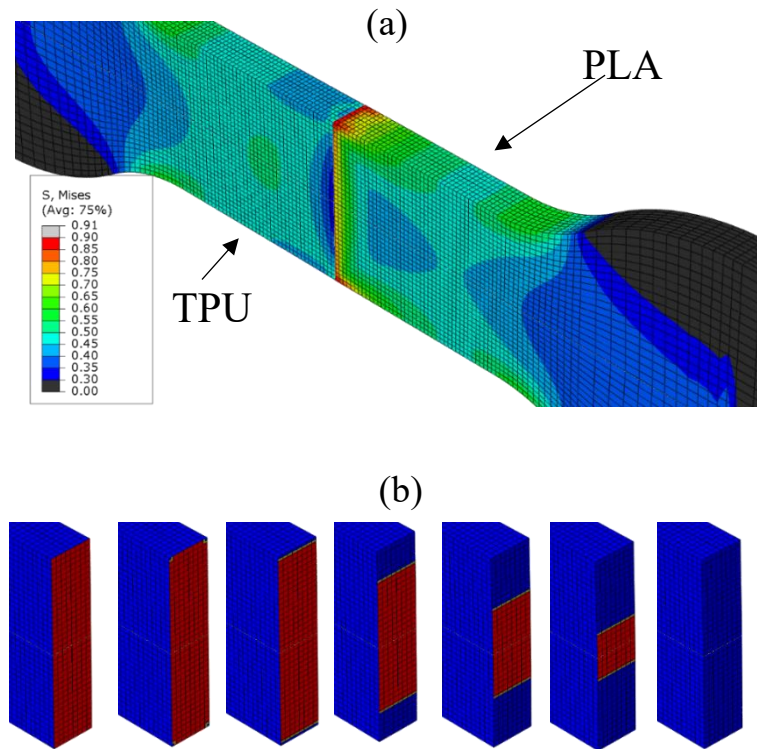


Figure 2.19. (a) The Von-Mises stress state of the flat interface specimen just before the crack initiation (b) Snippets showing the progression of the cohesive contact loss at interface surface of the TPU specimen. The red regions show a bonded contact, and the blue regions indicate those not in contact.

If the interface strength were set to 0.4 MPa, the corners would fail at that stress value then the crack would propagate to the center. Also, the engineering stress calculated for the specimen would be lower than 0.4 MPa as when corners reach 0.4 MPa, the average stress in the narrow region was smaller as the stress level at the corners is higher than in other regions. Therefore, the interface strength should be

higher, but 0.4 MPa could be used as an initial guess value for tensile damage initiation stress.

The test and the simulation stress-strain data of the flat interface specimen are given in Figure 2.20. The interface stiffness coefficients and damage initiation strength values are found. There is an acceptable difference in tensile strength, while the initial slope of the simulation is perfectly fitted.

The stiffness coefficient of the interface is found as 25 N/mm³, and the tensile strength or damage initiation stress is 0.66 MPa.

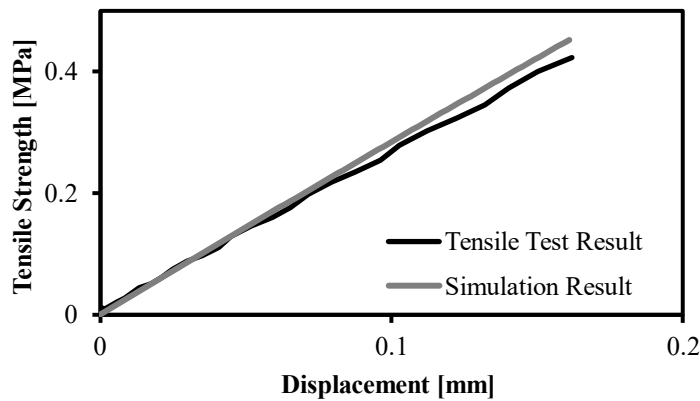


Figure 2.20 Tensile test result versus simulation result graph for TP0 specimen.

While modeling the shear test specimen, for the stiffness coefficient of the interface, the same value found in the TP0 simulations was used as a first iteration, which gave a good result. Thus, further iterations were not done for the stiffness estimation. The initial values for the tensile strength for both interfaces were set to 0.66 MPa, which gave lower UTS results for the specimen.

While tensile strength was set to 0.66 MPa, increasing the interface shear strength did not affect the stress-strain behavior of the part as the fracture occurred prematurely due to the tensile forces. When lower shear strength values were set, the

fracture occurred early again, which gave a low UTS value compared to the tensile test experiments.

The optimal tensile and shear strength values at the upper interface (as shown in Figure 2.7) that found for the tensile strength was 1.2 MPa where shear strength was 15 MPa for the, while tensile strength was found as 4 MPa and shear strength was found as 15 MPa for the lower interface.

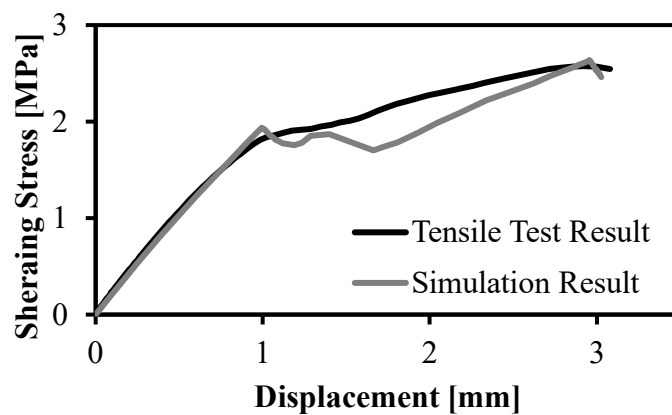


Figure 2.21. Tensile test result versus simulation result graph for the shear test specimen.

2.4 Conclusions

In this chapter, the influence of mechanical bonding on the mechanical performance of multi-material FFF 3D printed parts was investigated. Firstly, the mechanical properties of PLA and TPU materials were evaluated, then the multi-material printed parts composed of PLA and TPU were examined through uniaxial tensile tests.

The mechanical tests of flat interface and shear test specimens have shown that the PLA-TPU interface is not strong, and mechanical enhancement should be introduced to increase the overall strength of the multi-material printed part.

Comb-type intrusions with comb lengths 2, 4, and 6 mm were selected as the mechanical bonding method in this project. It was found that the comb length impacts the strength of the interface in a nonlinear fashion; that is, the longer the comb length, the effective it is. However, the effect of the comb length on the UTS was limited, and there was no improvement when the comb length increased from 4 to 6mm. On the other hand, increasing the comb length enhanced the elongation at break values. Therefore, the comb length for a FFF 3D printed part should be selected carefully, as increasing the comb length may cause a longer printing time.

The finite element method was used to model the uniaxial tensile tests for PLA, TPU, and multi-material flat interface and shear test specimens. It was found that the tensile strength of the interface cannot directly be deduced from the tensile test results as the fracture along the interface does not occur abruptly, but there were crack initiation and propagation phases. As future work, biaxial tensile tests will be done so that the Ogden model can be used with more confidence using the test results.

CHAPTER 3

CARBON FIBER-REINFORCED POLYAMIDE CELLULAR STRUCTURES PRODUCED BY FFF

3.1 Introduction

The mechanical performance of the parts produced through the FFF 3D printing method with virgin thermoplastic materials is not as strong as their injection-molded counterparts. Therefore, there is a need to increase the mechanical strength so that FFF 3D printing becomes a more appealing production method.

One of the main methods to increase the material strength is introducing strong fiber materials into the polymer matrix to obtain a composite structure; if the adhesion between the polymer and the fibers is at an acceptable level, the mechanical strength increases.

As the fiber addition into the polymer matrix does not positively affect all of the material properties, it is not possible to recommend printing all of the parts with CFRP filaments. Thus, the effect of the fiber additions on the material properties should be investigated to be able to select the suitable material for 3D printing a part.

In this part of the thesis, only the mechanical characterization on FFF 3D printed parts were done through tensile and compressive tests. The parts were printed with polyamide (Ultrafuse PA Natural – 2.85mm, BASF, Germany) and carbon fiber reinforced polyamide (Ultrafuse PAHT CF15 – 2.85mm, BASF, Germany) filaments. The CF filling amount to the polymer matrix in the PAHT CF15 filament is stated as 15% in the technical data sheet provided by the manufacturer.

3.2 Experimental details

3.2.1 Sample Preparation

The specimens were printed using an Ultimaker 3 Extended (Ultimaker BV, Netherlands) dual nozzle FFF 3D printer. The provided printing parameters for PAHT CF15 compressive test specimens and given in Table 3.1.

Table 3.1. FFF 3D printing parameters of compressive test specimens printed with PA and PAHT CF15 materials

Parameter	
Filament Diameter	2.85 mm
Nozzle Diameter (PA, PAHT CF15)	0.4, 0.6 mm
Layer Thickness	0.2 mm
Line Width (PA, PAHT CF15)	0.4, 0.8 mm
Printing Speed	55 mm/s
Nozzle Temperature (PA, PAHT CF15)	240 270 °C
Build Plate Temperature (PA, PAHT CF15)	105, 110 °C
Material Flow	100%

Before the tensile and compression tests, specimens were weighted to verify the printing repeatability and understand the weight and solid volume ratio dependency.

3.2.2 Uniaxial Tensile Testing

Uniaxial tensile tests were conducted to evaluate the mechanical properties of the polymer filaments. Three sets of tensile test specimens with 0°, 90° raster angles, and a concentric infill were prepared for each material type. The tensile tests were

conducted following the ASTM tensile test standards for plastic materials [89]. The test speed was selected as 5 mm/min, which is given in the mentioned standard.

Photographs of 3D printed PA and PAHT CF15 tensile test specimens are given in Figure 3.1. The raster orientations of the specimens were 0°, 90°, and concentric infill specimens have 0° raster angle in the narrow region.



Figure 3.1. Tensile test specimens printed with PA and PAHT CF15 filament and having 0°, 90° raster angles, and a concentric infill

3.2.3 Compressive Testing

The uniaxial compressive test is a versatile tool to understand the behavior of materials under compressive loads. In this work, compressive tests were done to examine the effect of the infill pattern and 3D printing filament material on the mechanical properties, especially the compressive strength of the products. There

were three main types of infill patterns printed with two different materials tested through the compressive tests.

Honeycomb, Voronoi, and gyroid infill patterns were used for compressive test specimens. For honeycomb and gyroid infills, specimens were printed with and without a wall; however, the Voronoi infill specimens had a wall structure. The pictures of printed specimens are given in Figure 3.2.

The volumetric density of the specimens was calculated using the mass of each specimen, m , and density of the filaments, ρ_{mat} , that the manufacturer provides. The width, length, and height of each compressive test specimen were measured to calculate their volume. Then using the calculated volume and density information obtained from the filament technical data sheet, the estimated weight of each is calculated as if they are printed with 100% infill using the equation (5).

$$m_{est} = \rho_{mat}V \quad (5)$$

The measured mass of each specimen was divided by each calculated 100% infill weight to calculate the volumetric density ρ_V , as shown in equation (6).

$$\rho_V = \frac{m}{m_{est}} \quad (6)$$

Then, the densification strain, ε_d , is found using equation (7).

$$\varepsilon_d = (1 - \rho_V) \quad (7)$$

All of the cellular structures were compressed up to their densification strain.

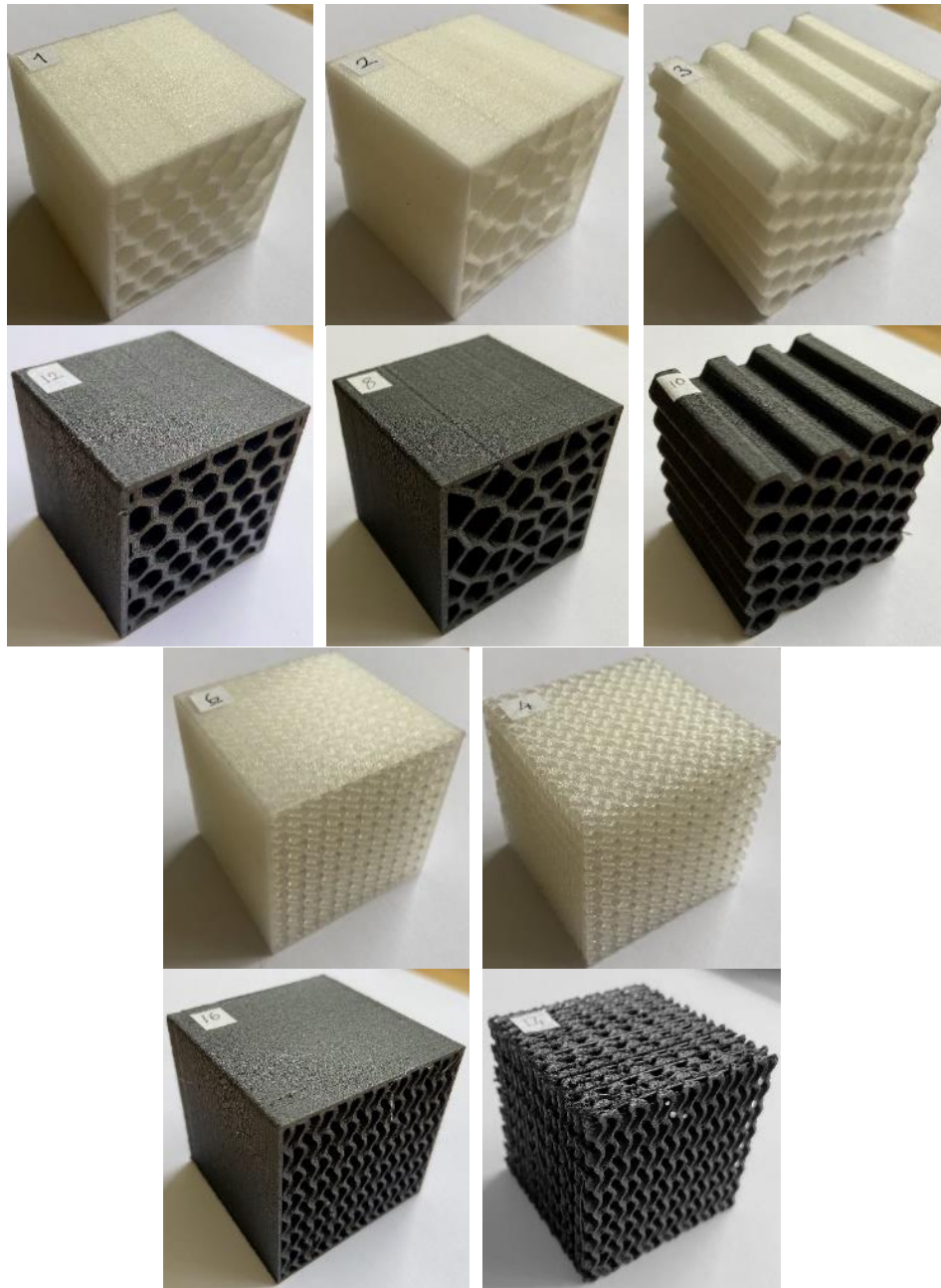


Figure 3.2. The compressive specimens printed with PA and PAHT CF15 filaments. The upper five specimens were printed with PA, and the specimens at the bottom were printed using PAHT CF15 material. The corresponding geometries are hexagonal with a wall, hexagonal without a wall, Voronoi, gyroid with a wall, and gyroid without wall from left to right and top to bottom, respectively.

The compressive tests were conducted using a uniaxial material testing machine (Z250, Zwick/Roell, Germany). Cross-head speed was 5 mm/min, calculated using the height of the compressive test specimens, which is the same as 10% strain per minute given in ASTM D1621-16 standard test method for compressive properties of rigid cellular plastics [93].

The compressive stress was calculated using equation (8), where σ_C is the compressive stress, F_C is the compressive force and A_C is the cross-sectional area.

$$\sigma_C = \frac{F_C}{A_C} \quad (8)$$

The yield strength of the compressive test specimens is found using the instructions given in the ASTM D1621-16 standard, which prescribes that the stress level at 10% strain is compared with all stress values in the strain history of the test until 10%, and the higher one is selected as the yield strength of the structure.

3.2.3.1 Energy Absorbance Efficiency

Materials having appropriate energy absorption properties are needed in the industry for various purposes, e.g., to protect a delicate instrument while it is being shipped. Customized energy absorbers are needed since various devices having different weights and densities need to be cushioned.

Primarily, foams having different densities are used as energy absorbers. As the foams have a pseudo-stochastic structure, the mechanical properties of the foams are tuned by producing them using different materials or altering the relative density. However, by introducing the possibility of designing parts with internal cavities and different infill patterns, the AM enables the production of parts designed to exhibit specific energy absorption characteristics [94]. By utilizing 3D printing methods, it

is possible to obtain a structure having mechanical properties almost as good as the ideal energy absorber [95].

For an ideal energy absorber, the plateau stress should be kept at the same level until the compressive strain reaches the unity so that the energy is absorbed in a constant, reliable rate. The stress versus strain response of an ideal energy absorber is given in Figure 3.3.

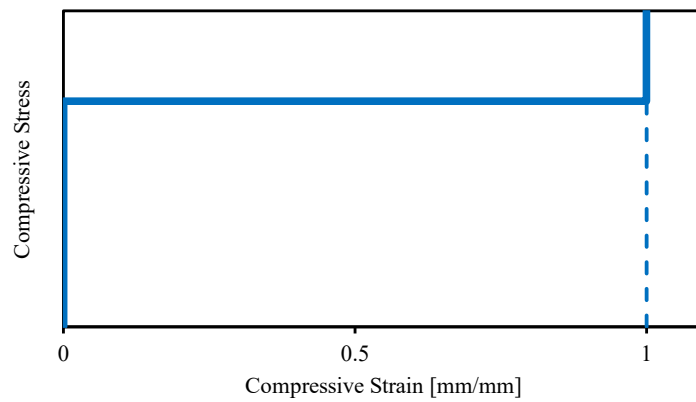


Figure 3.3. Stress versus strain response of an ideal energy absorber.

There are several methods to quantify the properties of energy absorbers, and one of them is drawing the absorbed energy per unit volume versus peak stress diagram. The peak stress, σ_p , is the stress value that is the maximum stress that is calculated throughout the loading history until specified strain level. The initial value assigned to the peak stress is 0, and the peak stress values for all strain values are calculated using the equation (9).

$$\sigma_p(\varepsilon) = \begin{cases} \sigma(\varepsilon) & \text{if } \sigma(\varepsilon) > \sigma_p(\varepsilon) \\ \sigma_p(\varepsilon) & \text{if } \sigma(\varepsilon) \leq \sigma_p(\varepsilon) \end{cases} \quad (9)$$

The absorbed energy per unit volume, W , is calculated using equation (10) and plotted for each infill type versus peak stress value [96].

$$W = \int_0^{\varepsilon} \sigma_c(\varepsilon) d\varepsilon \quad (10)$$

For an ideal energy absorber, the graph is given in Figure 3.4.

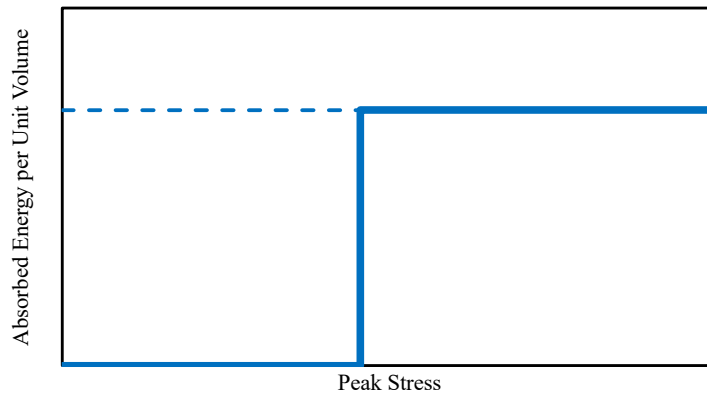


Figure 3.4. Absorbed energy per unit volume versus peak stress diagram of an ideal energy absorber.

Another method for measuring the energy absorber characteristics is calculating the energy absorption efficiency. The energy absorption efficiency, η , was calculated using equation (11) [96].

$$\eta(\varepsilon) = \frac{\int_0^{\varepsilon} \sigma(\varepsilon) d\varepsilon}{\sigma_p(\varepsilon)} \times 100 \quad (11)$$

In this equation, the energy absorber is compared to its ideal counterpart with plateau stress as the peak stress of the calculated absorber for each strain level. Using the absorbed energy and energy absorption efficiency values makes it possible to compare the compressive performance of different material and infill geometry conditions. The absorbed energy efficiency versus compressive strain for an ideal energy absorber is given in Figure 3.5.

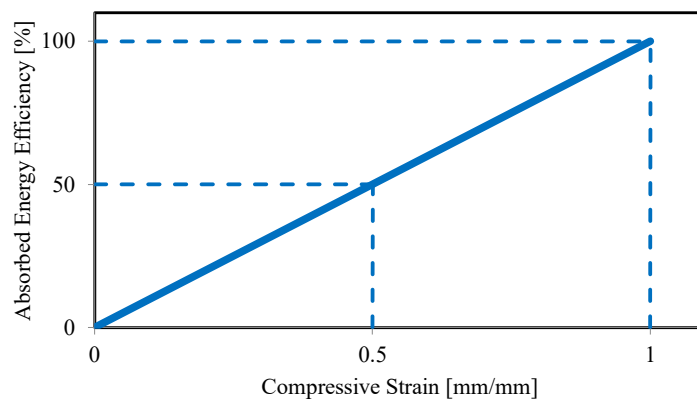


Figure 3.5 Absorbed energy efficiency versus compressive strain graph for an ideal energy absorber.

3.3 Results and Discussion

3.3.1 Tensile Testing

Tensile test results of specimens produced using PAHT CF15 material revealed that tensile modulus and strength strongly depend on the raster orientation, as shown in Figure 3.6. When 0° raster angle specimens were compared, even though the infill pattern drastically changed in the contraction region for concentric specimen, the effect of the infill pattern on mechanical properties found from the uniaxial tensile tests was negligible.

Since printing with concentric infill may reduce printing time and enables to print specimens more smoothly while the mechanical test results do not differ much compared to 0° raster angle specimens, only concentric infill specimens can be used for further tests to assess the mechanical properties of PAHT CF15 tensile test specimens with a 0° raster angle.

The difference in tensile modulus and tensile strength of 0° and 90° raster angle specimens is also evident, which shows that PAHT CF15 specimens exhibited anisotropic mechanical behavior in terms of these parameters. The high tensile strength and modulus values of 0° raster angle specimens show that the chopped CF additions might be aligned along with the printing direction, which improved the mechanical properties better in that direction compared to 90° raster angle specimens.

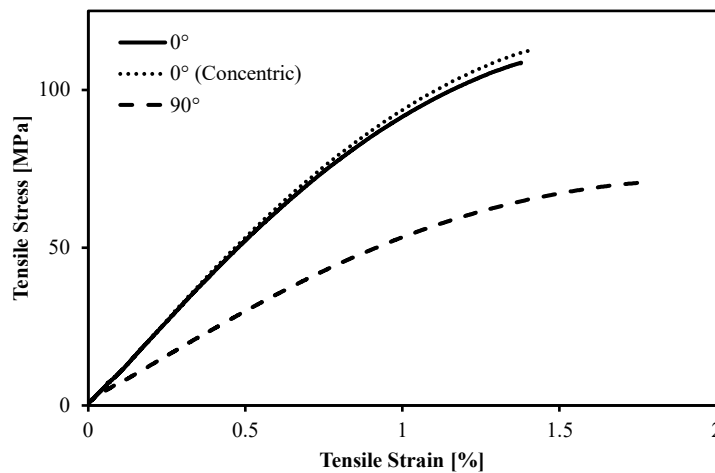


Figure 3.6. Tensile stress versus tensile strain plot of PAHT CF15 specimens for concentric infill, 0°, and 90° raster angles.

Contrary to the test results of specimens printed with PAHT CF15, in the case of PA specimens, in concentric infill, the ductility decreased sharply compared to the 0°

raster angle. The tensile test results of PA specimens have also shown that the elongation at the break value of the specimens was also strongly dependent on the raster orientation, as 90° raster angle specimens displayed very low plastic deformation whereas 0° raster angle specimens experienced plastic deformation after yielding.

As can be seen in Figure 3.7, the tensile modulus does not differ in PA specimens for different infill geometries and raster angles. Therefore, it can be inferred that the raster orientation dependency of mechanical properties in PAHT CF15 specimens was due to the CF reinforcement.

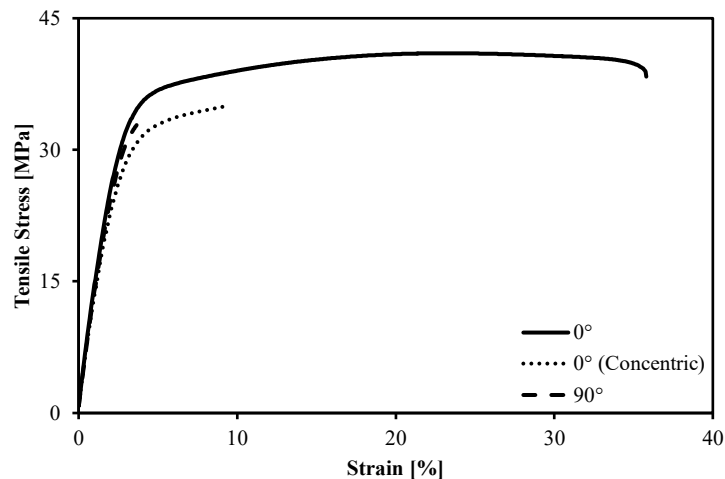


Figure 3.7. Tensile test results of PA specimen tensile test specimens, for concentric infill, 0°, and 90° raster angles.

The investigation of the PA and CF reinforced PA specimens shows that, with the CF addition, the tensile strength of parts was significantly increased while elongation at break values notably decreased.

The optical microscopy images showing the top surface of a concentric infill PAHT CF15 tensile test specimen are given in Figure 3.8. Even though it seems the fibers

were randomly placed, a closer look at the microscopy photos shows the alignment of the carbon fibers. The preferred orientation of the carbon fibers was along the printing direction, which is visible in these pictures. The alignment of the fibers explains the anisotropic behavior seen in the PAHT CF15 tensile test specimens.

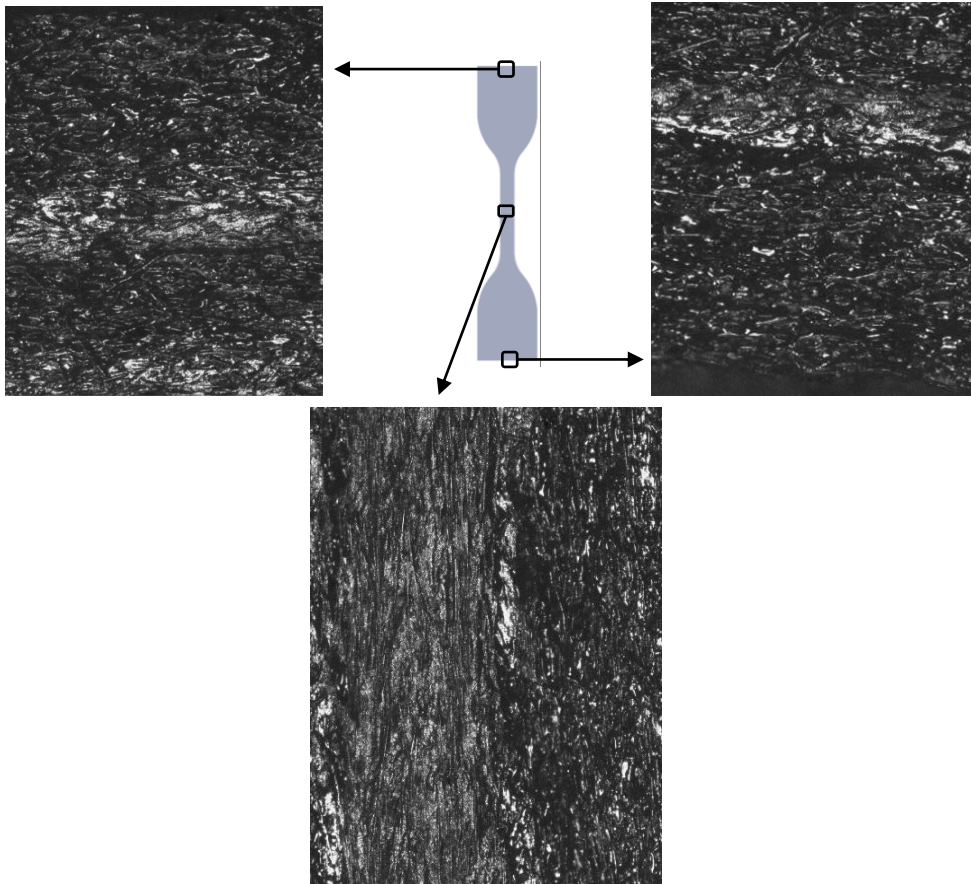


Figure 3.8. The optical microscopy image showing the top surface of a concentric infill tensile test specimen.

A picture of fractured PAHT CF15 tensile test specimens having 0° , 90° raster angles and a concentric infill is given in Figure 3.9. As in accordance with the stress-strain curve given in Figure 3.6, it was observable that the fractures occurred in a brittle manner since there was no visible elongation around the fracture region. The

decrease in ductility might stem from the potential crack sites created by the CF reinforcement. Therefore, the filament materials for 3D FFF printing should be selected according to the use conditions of the printed parts due to this ductility and strength tradeoff.



Figure 3.9. The fractured tensile test specimens printed with PAHT CF15 and having 0°, 90° raster angles, and a concentric infill.

When the tensile modulus of the specimens printed with the PA and PAHT CF15 filaments are compared in Figure 3.10, it can be seen that the modulus of the parts printed with CF reinforced filaments are much higher. Furthermore, in terms of tensile modulus, the PA specimens exhibited isotropic behavior, whereas the PAHT CF15 specimens were anisotropic. The standard deviation values are shown with the error bars, which are considerably low for each case.

The UTS of the PAHT CF15 tensile test specimens is found to be higher than that of PA specimens, which can be seen from Figure 3.10. The error values in the UTS values were considerably low. The PAHT CF15 specimens show dependence on the raster angle such that the UTS value decreased sharply when the raster angle was 90°.

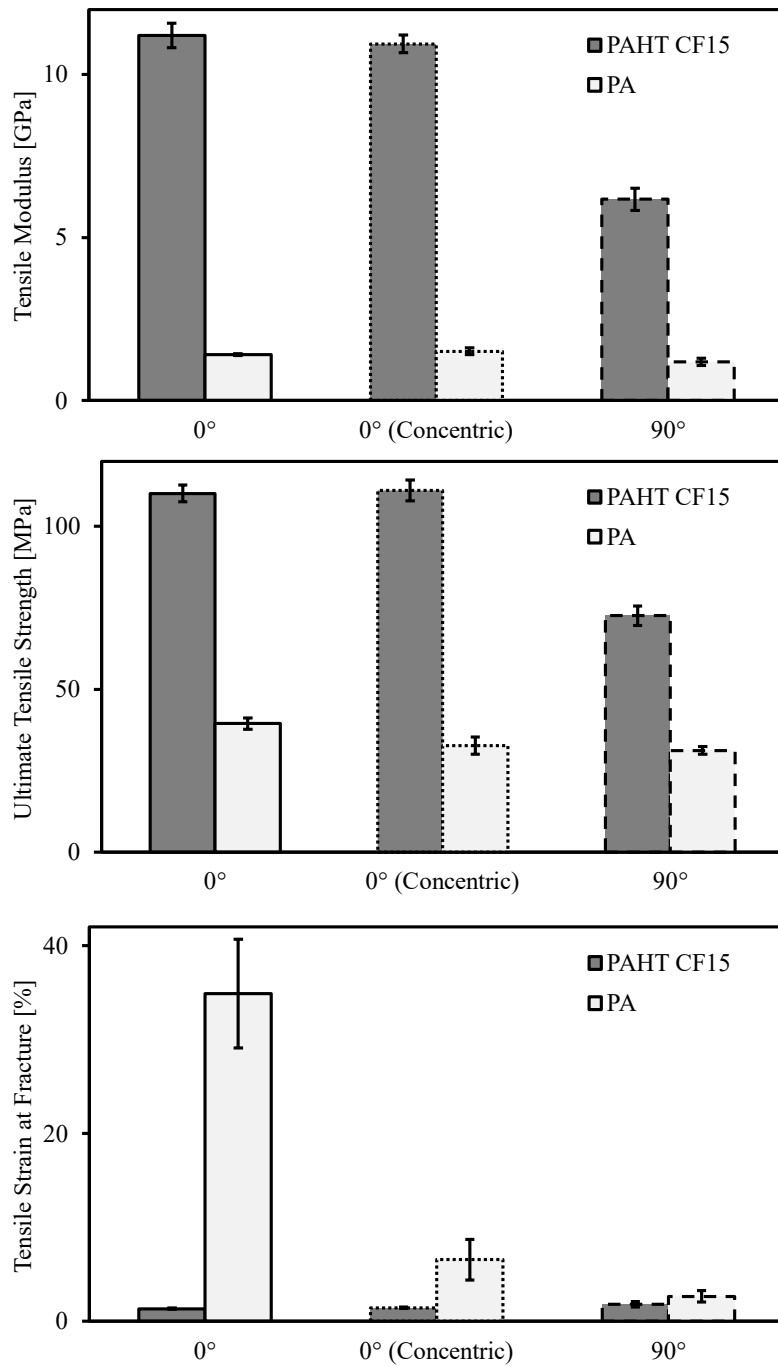


Figure 3.10. Tensile modulus, ultimate tensile strength, and tensile strain at fracture values of the PA and PAHT CF15 specimens for concentric infill, 0°, and 90° raster angles.

The tensile strain at fracture values is given in Figure 3.10. PAHT CF15 specimens have much less fracture strain than the PA specimens, where the difference is more visible compared to the difference in tensile modulus and the UTS values.

Interestingly, even though the modulus and UTS values do not differ much with the infill type, the change in fracture strain is more visible in PA specimens. It should also be noted that even though the raster angles in the narrow region were the same in the concentric infill and 0° raster angle, the fracture strain value drops drastically in concentric infill specimens.

The fracture strain of the PAHT CF15 specimens in the investigated three infill types does not differ as in the tensile modulus and UTS. It should be noted that, however, contrary to the parts printed with PA, the fracture strain values go up when the raster angle is 90°.

As the mechanical properties of the FFF 3D printed PA and PAHT CF15 materials depend on the raster orientation, the raster orientation of printed parts should be chosen wisely in the design phase to maximize the strength.

3.3.2 Compressive Testing

The stress-strain response of honeycomb, gyroid, and Voronoi infill PA and PAHT CF15 specimens printed both with or without a wall around the infill structure are given in Figure 3.11 together and Figure 3.12 separately. Honeycomb infill was shown with black, gyroid with gray, and Voronoi with red colors. The specimens printed with wall shown with full line whereas unwalled specimens were shown with dashed lines. The PAHT CF15 specimens were shown with darker whereas PA specimens were designated with lighter colors.

Two specimens were tested in each material, infill, and wall configuration set when it is possible to quantify the repeatability. When the results of those specimens are investigated, it is seen that the error of the experiment is deficient in especially yield strength and compressive modulus values.

In Figure 3.11, one specimen from each set is shown to decrease the data shown to avoid complications. It is easy to compare each compressive test specimen with others using this figure. The first observation was an increase in compressive yield strength when the wall structure was included around the infill for honeycomb and gyroid specimens. It was also seen that PAHT CF15 specimens had higher compressive modulus and yield strength for all the parts.

The investigation of unloading regions, occurred after the densification strain illustrates that the permanent deformation in the PAHT CF15 specimens was more than the PA specimens.

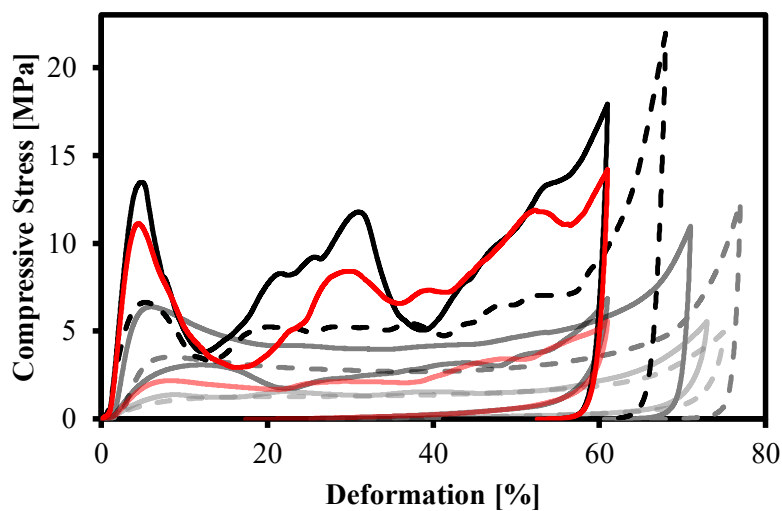


Figure 3.11. Compressive test results of the honeycomb (black), gyroid (gray), and Voronoi (red) infill patterns for both PA and PAHT CF15 specimens.

Figure 3.12 (i) shows the two PAHT CF15 honeycomb specimens were tested for with and without wall configurations. It is noteworthy that the yielding strength and strain are almost precisely the same. However, the stress-strain behavior in the post-

yielding region is different, and in fact, seemingly random, which may be caused by the imperfections caused in the production of the test pieces.

As for gyroid specimen sets shown in Figure 3.12 (ii), two specimens were tested for each configuration. Similar to the honeycomb specimens, the compressive modulus and yield strength values are almost identical for each set.

Unlike the case in honeycomb specimens, after the yielding, the stress-strain response of the specimens in the same set was almost the same in gyroid specimens. The smooth response in the post-yielding area is the 3D shape of the gyroid infill type, which does not allow sudden buckling behavior.

Three Voronoi test specimens were tested as shown in Figure 3.12 (iii), one produced with PA and two PAHT CF15 materials using identical geometry. The test pieces printed with reinforced filaments showed that there is good repeatability, with almost identical compressive modulus and yield strength.

After the yielding, the behavior of these two pieces is almost the same, with minor fluctuations. The reason for that is the unique Voronoi shape created for the experiment. Thus, it might be said that the Voronoi infill geometry can be tailored to meet a specific demand in terms of mechanical response. It is also seen that, when there is no CF reinforcement, the compressive strength of the Voronoi infill geometry is meager, and the stress response is flatter after yielding.

The strain recovery during the unloading goes up to 30% deformation for all PA compressive test specimens, whereas the PAHT CF15 specimens do not exhibit that much of a recovery. Also, the slope drawn in the start of the unloading is steep in PAHT CF15 specimens, showing there was almost no room for energy absorption capacity for that stress level. Moreover, there is reusable elastic energy in the PA compression specimen, which may be required for specific applications where multiple loading and unloading occur.

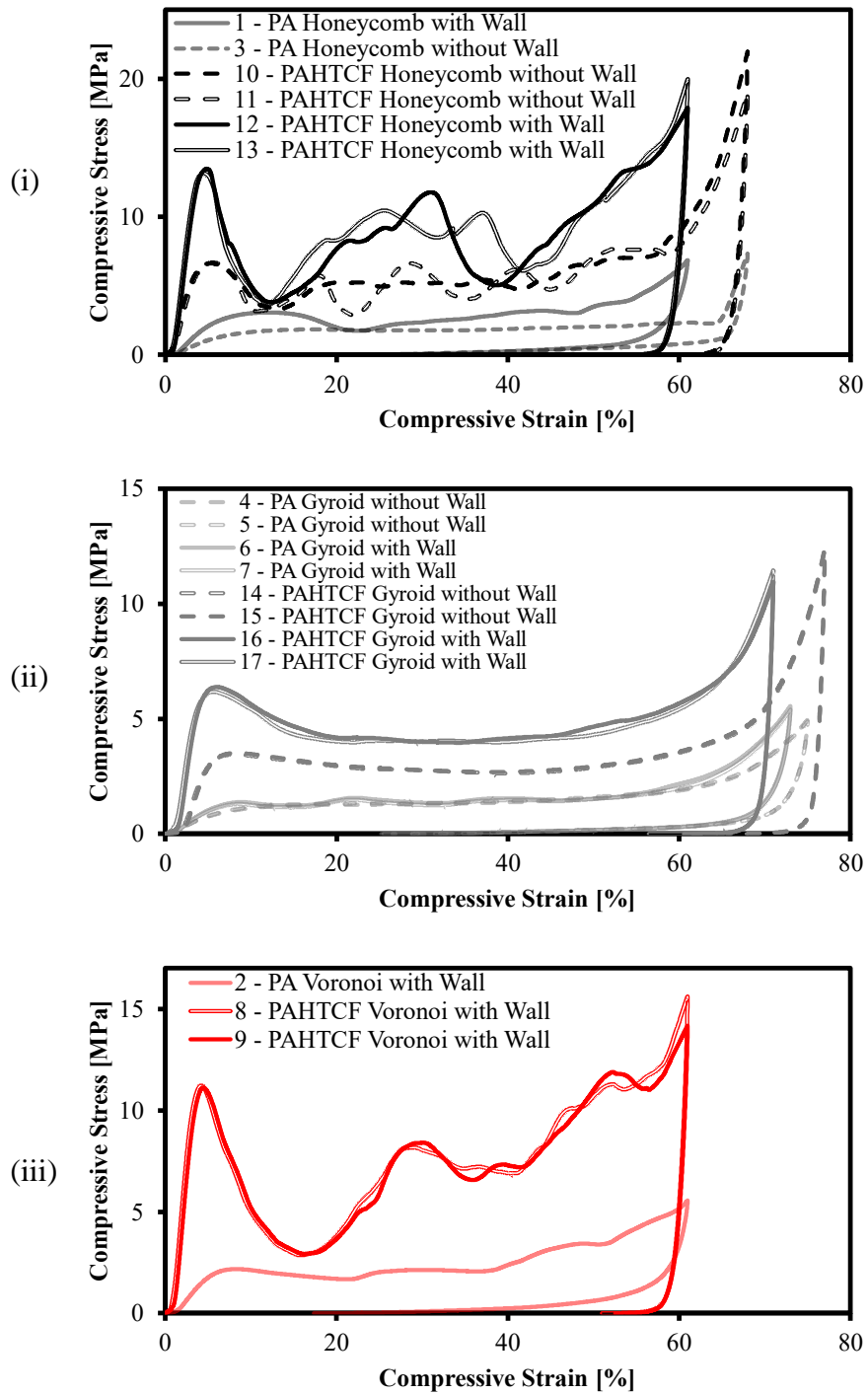


Figure 3.12. Compressive test results of (i) honeycomb, (ii) gyroid, (iii) Voronoi infill patterns for both PA and PAHT CF15 materials.

3.3.3 Energy Absorption and Efficiency

For all of the specimens, the effect of the material is highly evident, as can be seen in Figure 3.13, as the peak stress and maximum absorbed energy values are increased for all specimens. Therefore, for more strength-demanding purposes, PAHT CF15 material can be utilized instead of neat PA.

The effect of a wall structure is noticeable in both honeycomb and gyroid specimens. Adding a wall structure increased both peak stress and absorbed energy for all, except the PA gyroid specimens. In that case, however, the smooth transition of peak stress value was changed to a steep peak stress behavior.

In honeycomb specimens, it is seen that in Figure 3.13, when the wall is introduced, both the stress level that is needed to compress the structure and the effective absorption capacity increases for both materials. The effect of the material can be clearly seen, as both absorbed energy and peak stress values are considerably high in PAHT CF15 specimens.

The influence of the wall in the case of gyroid infill specimens is not evident when the material is PA as neither the absorbed energy nor the stress level needed to be achieved to crush the structure. Nevertheless, it should be noted that introducing the wall causes the peak stress value to sustain at a value. On the other hand, in PAHT CF15 specimens, the effect of the wall is noticeable as both properties were increased.

In the case of the specimens having a Voronoi infill pattern, there was no variation in terms of the wall, i.e., all parts are printed with the wall structure. The only changing parameter was the material, which affected the results as the other infill materials, increasing both the peak stress and absorbed energy.

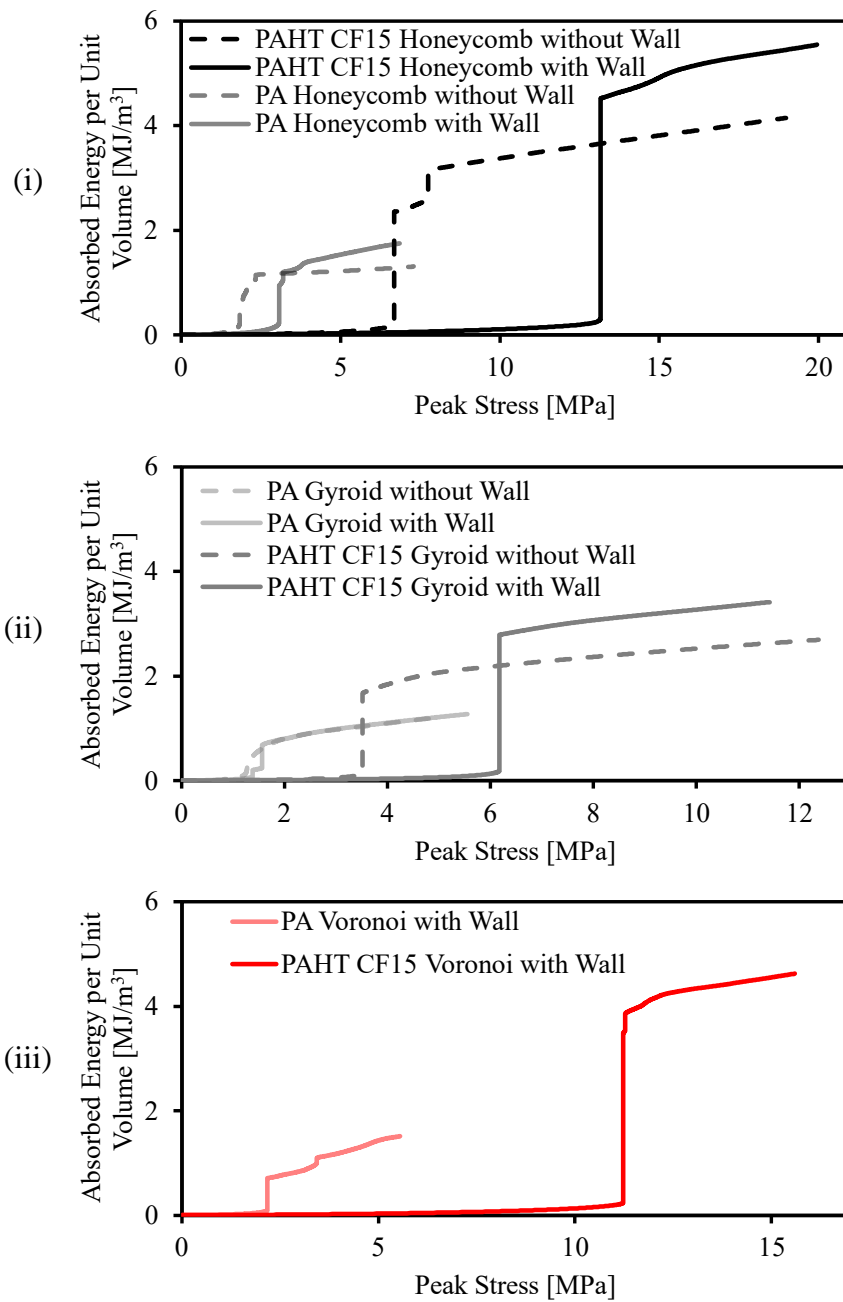


Figure 3.13. Peak stress versus absorbed energy per unit volume graph of compressive test specimens printed using (i) honeycomb, (ii) gyroid, and (iii) Voronoi infill with and without wall.

Compressive modulus, compressive yield strength, and maximum energy absorption efficiency values of each compressive specimen set were given in Table 3.2. The numerical values given in the table further illustrate the beforementioned factors, such as infill pattern and printing material, that influence the mechanical performance. The compression modulus was strongly affected by the wall structure and the printing material. For all specimen sets, the specimens printed with PAHT CF15 material have 10-folds of compressive modulus values compared to the PA specimens.

Additionally, it was observed that the compressive yield strength of the structure was not definitive for the energy absorption efficiency. A closer look at the table shows that the parts having the same efficiency values, namely PAHT CF15 honeycomb without wall and PA gyroid without wall, have remarkably different yield strength values, 6.66 and 1.14 MPa, respectively.

In terms of the energy absorption efficiency, the effect of the wall structure was standing out. When the wall was introduced, the efficiency values dropped sharply for honeycomb specimens, as wall structure restricts the deformation of the cellular structure. There were voids around the regions connected to the wall at the top and bottom sections. Also, there were squeezed regions around the buckled side walls, hindering the energy absorption efficiency as compressive stress increased due to the squeezed partitions.

When all compressive test specimens were investigated, it was found that the maximum efficiency is 49%, found in the PA honeycomb infill specimen printed without a wall. The second one was the PAHT CF15 gyroid infill specimen printed without a wall, having a 48% efficiency. The minimum efficiency value is found as 34% in the PA Voronoi specimen.

Table 3.2. The compressive modulus, compressive yield strength, and maximum energy absorption efficiency values of the different compressive test specimens

Specimens	E_C [MPa]	σ_Y [MPa]	η [%]
PA Honeycomb with Wall	51.19	3.02	38
PA Honeycomb without Wall	25.88	1.65	49
PAHT CF15 Honeycomb with Wall	527.53	13.31	34
PAHT CF15 Honeycomb without Wall	240.62	6.66	41
PA Gyroid with Wall	25.29	1.34	44
PA Gyroid without Wall	18.43	1.14	41
PAHT CF15 Gyroid with Wall	253.21	6.28	45
PAHT CF15 Gyroid without Wall	113.38	3.48	48
PA Voronoi with Wall	49.29	2.18	33
PAHT CF15 Voronoi with Wall	461.10	11.17	35

Figure 3.14 shows the stress and efficiency versus tensile strain graph of best and worst-performing compressive test specimens. The values in horizontal and both vertical axes are selected to be equal so that they can be compared easily.

It was remarkable that even though both specimens were compressed to a similar maximum compressive strain level, their efficiency values differed significantly. Therefore, the volumetric density of the material is not the only effective parameter, but the infill pattern also plays a vital role in the absorbed energy efficiency parameter.

It should be noted that, however, in terms of the maximum absorbed energy of these two specimens, Voronoi infill specimen was better, absorbing 1.51 MJ/m^3 , whereas the honeycomb infill absorbed 1.31 MJ/m^3 . Hence, for a tightly packed area, the Voronoi infill specimen would absorb more energy.

When their energy absorption values are divided by their density, the energy absorption value per kilograms can be found. In this regard, the honeycomb infill

specimen outperformed the Voronoi structure. Therefore, if the weight or amount of cellular structure material used in the design is concerned, the honeycomb infill specimen could be selected as an energy absorber.

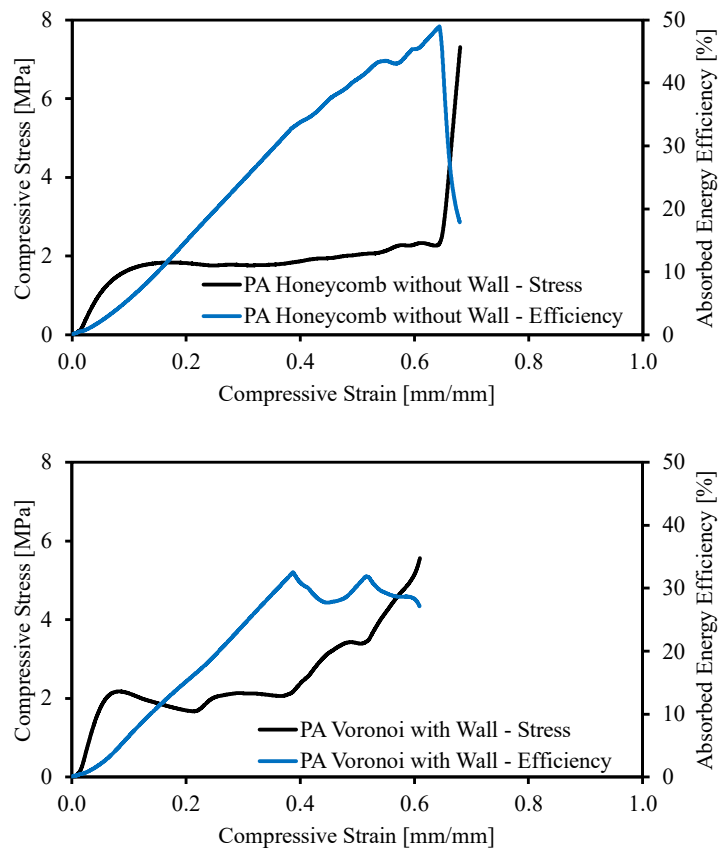


Figure 3.14. The compressive stress and absorbed energy efficiency versus strain plot of best and worst-performing specimens. The PA Voronoi specimen was printed without a wall, and the PA Honeycomb specimen was printed without a wall, shown on top and bottom, respectively.

The test videos were shot during the compressive tests, and snippets from the videos were given in Figure 3.15, which further support the mentioned results. First, it is seen that the Honeycomb infill specimen is compressed regularly, such that the

compressed regions and voids are dispersed evenly. As there was no wall structure and no vertical or relatively long edges, the buckling failure was not observed, resulting in a smooth curve after the yielding.

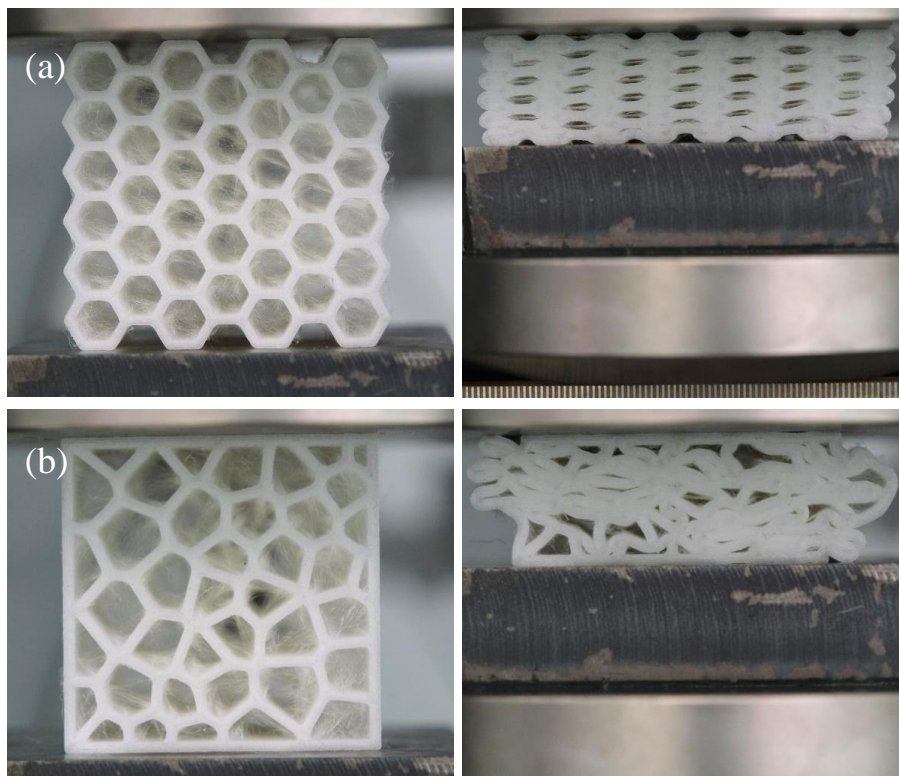


Figure 3.15. The photographs of the (a) best and (b) worst performing specimens. These were taken from the test video shot during the compressive test

The Voronoi infill specimen has the lowest efficiency value, which stemmed from several reasons seen in the compressed Voronoi infill specimen photograph. There were irregular voids and squeezed regions, which is the main reason for the low efficiency. Also, the buckled regions were observable, especially at the top-right section of the specimen, which caused the stepped behavior after the yielding of the specimen. It is also evident that the material close to the top and bottom portions

were not displaced; therefore, they were not effective in absorbing the compressive energy.

3.4 Conclusions

Both the tensile modulus and the strength of the PAHT CF15 specimens were higher than the PA specimens. However, the PAHT specimens CF15 exhibited anisotropy in mechanical properties, which shows that the fibers were oriented along the printing direction. The parts printed with CF reinforced filaments showed low ductility compared to those printed with PA filaments, which may be caused by the crack initiation sites in the polymer and carbon fiber interface.

The tensile tests results of the PAHT CF15 specimens revealed that the tensile modulus of the 0° raster angle specimens almost doubled the 90° specimens. Similarly, the UTS values show a visible positive change, whereas strain at fracture values of the 90° raster angle specimens was higher than 0°.

Compressive test specimens having three different infill patterns were printed with PA and PAHT CF15 filaments. The results show that it was possible to obtain an energy absorber tuned to the required use conditions. The infill pattern, use of the wall, and material type affect the energy absorption characteristics of the FFF 3D printed parts.

The PAHT CF15 specimens outperformed the PA specimens in terms of the compressive strength and modulus values. However, during the unloading, the PA specimens performed better as they had a more gradual unloading curve, which shows that they can absorb energy even after being compressed to their densification strain.

Using a wall structure increased the compressive strength and modulus but caused stress fluctuations in the plateau region due to the buckling of the wall. A wall structure can be introduced to the cellular structures if a higher compressive yield

strength and compressive modulus are needed. Nevertheless, it should be noted that there might be fluctuations in the plateau region.

Finally, it was found that irregular infill type, Voronoi, was performed inferior to honeycomb infill specimen, which has a regular infill pattern. Moreover, in terms of maximum absorbed energy, the Voronoi specimen was better in terms of volumetric efficiency, whereas the honeycomb was better in terms of absorbed energy per cellular structure mass. Hence, even comparing the best and worst-performing cellular structures in terms of energy absorption efficiency is quite tricky, and attention is needed in the design phase while selecting a proper infill pattern for energy absorbers.

CHAPTER 4

CONCLUSIONS AND FUTURE WORK

Compared to the earlier days of rapid prototyping, AM methods now play a more vital role in producing prototypes and actual components, thanks to the developments in AM technology and methods. Even though most of the materials and process parameters used in FFF are investigated thoroughly in the literature, there are still gaps, especially for multi-material printing and reinforced filament materials. Two types of composite structures were investigated in-depth to understand their mechanical behavior and evaluate their mechanical properties.

Firstly, the mechanical properties of PLA and TPU interface were investigated through tensile tests done on in-house designed and 3D printed multi-material dogbone specimens. It was observed that the PLA and TPU materials do not firmly adhere to each other. The comb-like intrusions were effectively increased the overall strength of the FFF 3D printed multi-material parts. Therefore, to increase the overall strength of the printed part, a mechanical bonding method should be used in PLA-TPU interfaces. FEM method is utilized to understand the mechanical properties better and visualize the stress state of the 3D printed elastomer-plastic parts.

Secondly, polyamide and carbon fiber reinforced polyamide tensile dogbone, and cellular structure specimens were tested. It was found that the infill pattern plays a vital role in both tensile and compressive loading conditions for both PA and CF reinforced PA specimens. Carbon fiber additions to the polymer matrix increase the tensile modulus and UTS while reducing the elongation at break values of the 3D printed parts. It was also found that the CF reinforcement introduced anisotropy into the mechanical properties due to the preferred orientation of the fibers.

The energy absorption characteristics of a part printed by the FFF 3D printing method are affected by printing parameters and material type. The regular infill

pattern performed better in terms of energy absorption characteristics compared to the irregular Voronoi infill type. Therefore, it is possible to tweak these parameters to obtain a structure to meet a specific need.

In the future, different interlocking patterns can be designed to investigate enhancement to the interface strength through more involved mechanical locking. For a start, comb-type interlocking patterns having various taper angles can be designed and tested to evaluate the effect of the taper angle on the interface strength.

As interlocking geometries are needed to be introduced for printing multi-material parts with dissimilar filaments, it is needed to change the part geometry to an interlocking pattern, which is not only time consuming, but also may require altering the original part geometry. A novel slicing technique can be developed to automatize this process, such that the slicing software creates comb-like intrusions automatically to avoid these problems.

Lastly, compressive strain rate dependency of the FFF 3D printed energy absorbers can be investigated to increase their use cases. Also, utilizing multi-material printing, the energy absorbers can be fine-tuned further by combining compliant and stiff materials in a cellular structure.

REFERENCES

- [1] T. Pereira, J.V. Kennedy, J. Potgieter, A comparison of traditional manufacturing vs additive manufacturing, the best method for the job, *Procedia Manuf.* 30 (2019) 11–18. <https://doi.org/10.1016/j.promfg.2019.02.003>.
- [2] B.P. Conner, G.P. Manogharan, A.N. Martof, L.M. Rodomsky, C.M. Rodomsky, D.C. Jordan, J.W. Limperos, Making sense of 3-D printing: Creating a map of additive manufacturing products and services, *Addit. Manuf.* 1–4 (2014) 64–76. <https://doi.org/10.1016/j.addma.2014.08.005>.
- [3] T. Peng, K. Kellens, R. Tang, C. Chen, G. Chen, Sustainability of additive manufacturing: An overview on its energy demand and environmental impact, *Addit. Manuf.* 21 (2018) 694–704. <https://doi.org/10.1016/j.addma.2018.04.022>.
- [4] A. García-Dominguez, J. Claver, M.A. Sebastián, Integration of Additive Manufacturing, Parametric Design, and Optimization of Parts Obtained by Fused Deposition Modeling (FDM). A Methodological Approach, *Polymers.* 12 (2020) 1993. <https://doi.org/10.3390/polym12091993>.
- [5] A. Haleem, M. Javaid, Additive Manufacturing Applications in Industry 4.0: A Review, *J. Ind. Integr. Manag.* 04 (2019) 1930001. <https://doi.org/10.1142/S2424862219300011>.
- [6] J. Faludi, C. Bayley, S. Bhogal, M. Iribarne, Comparing environmental impacts of additive manufacturing vs traditional machining via life-cycle assessment, *Rapid Prototyp. J.* 21 (2015) 14–33. <https://doi.org/10.1108/RPJ-07-2013-0067>.
- [7] M. Attaran, The rise of 3-D printing: The advantages of additive manufacturing over traditional manufacturing, *Bus. Horiz.* 60 (2017) 677–688. <https://doi.org/10.1016/j.bushor.2017.05.011>.
- [8] D. Bourell, J.P. Kruth, M. Leu, G. Levy, D. Rosen, A.M. Beese, A. Clare, Materials for additive manufacturing, *CIRP Ann.* 66 (2017) 659–681. <https://doi.org/10.1016/j.cirp.2017.05.009>.

- [9] D. Han, H. Lee, Recent advances in multi-material additive manufacturing: methods and applications, *Curr. Opin. Chem. Eng.* 28 (2020) 158–166. <https://doi.org/10.1016/j.coche.2020.03.004>.
- [10] S. Upcraft, R. Fletcher, The rapid prototyping technologies, *Assem. Autom.* 23 (2003) 318–330. <https://doi.org/10.1108/01445150310698634>.
- [11] A. Bandyopadhyay, B. Heer, Additive manufacturing of multi-material structures, *Mater. Sci. Eng. R Rep.* 129 (2018) 1–16. <https://doi.org/10.1016/j.mser.2018.04.001>.
- [12] I. Ribeiro, F. Matos, C. Jacinto, H. Salman, G. Cardeal, H. Carvalho, R. Godina, P. Peças, Framework for Life Cycle Sustainability Assessment of Additive Manufacturing, *Sustainability.* 12 (2020) 929. <https://doi.org/10.3390/su12030929>.
- [13] J. Liu, A.T. Gaynor, S. Chen, Z. Kang, K. Suresh, A. Takezawa, L. Li, J. Kato, J. Tang, C.C.L. Wang, L. Cheng, X. Liang, Albert.C. To, Current and future trends in topology optimization for additive manufacturing, *Struct. Multidiscip. Optim.* 57 (2018) 2457–2483. <https://doi.org/10.1007/s00158-018-1994-3>.
- [14] M. Orme, I. Madera, M. Gschweidl, M. Ferrari, Topology Optimization for Additive Manufacturing as an Enabler for Light Weight Flight Hardware, *Designs.* 2 (2018) 51. <https://doi.org/10.3390/designs2040051>.
- [15] V. Kandemir, O. Dogan, U. Yaman, Topology optimization of 2.5D parts using the SIMP method with a variable thickness approach, *Procedia Manuf.* 17 (2018) 29–36. <https://doi.org/10.1016/j.promfg.2018.10.009>.
- [16] G.W. Melenka, J.S. Schofield, M.R. Dawson, J.P. Carey, Evaluation of dimensional accuracy and material properties of the MakerBot 3D desktop printer, *Rapid Prototyp. J.* 21 (2015) 618–627. <https://doi.org/10.1108/RPJ-09-2013-0093>.
- [17] U.M. Dilberoglu, B. Gharehpapagh, U. Yaman, M. Dolen, The Role of Additive Manufacturing in the Era of Industry 4.0, *Procedia Manuf.* 11 (2017) 545–554. <https://doi.org/10.1016/j.promfg.2017.07.148>.

- [18] T.D. Ngo, A. Kashani, G. Imbalzano, K.T.Q. Nguyen, D. Hui, Additive manufacturing (3D printing): A review of materials, methods, applications and challenges, *Compos. Part B Eng.* 143 (2018) 172–196. <https://doi.org/10.1016/j.compositesb.2018.02.012>.
- [19] K.R. Ryan, M.P. Down, C.E. Banks, Future of additive manufacturing: Overview of 4D and 3D printed smart and advanced materials and their applications, *Chem. Eng. J.* 403 (2021). <https://doi.org/10.1016/j.cej.2020.126162>.
- [20] L. Hirt, A. Reiser, R. Spolenak, T. Zambelli, Additive Manufacturing of Metal Structures at the Micrometer Scale, *Adv. Mater.* 29 (2017) 1604211. <https://doi.org/10.1002/adma.201604211>.
- [21] S. Lim, R.A. Buswell, T.T. Le, S.A. Austin, A.G.F. Gibb, T. Thorpe, Developments in construction-scale additive manufacturing processes, *Autom. Constr.* 21 (2012) 262–268. <https://doi.org/10.1016/j.autcon.2011.06.010>.
- [22] H. Bikas, P. Stavropoulos, G. Chryssolouris, Additive manufacturing methods and modeling approaches: A critical review, *Int. J. Adv. Manuf. Technol.* 83 (2016) 389–405. <https://doi.org/10.1007/s00170-015-7576-2>.
- [23] A.A. Bakır, R. Atik, S. Özerinç, Mechanical properties of thermoplastic parts produced by fused deposition modeling: a review, *Rapid Prototyp. J.* 27 (2021) 537–561. <https://doi.org/10.1108/RPJ-03-2020-0061>.
- [24] N. Volpato, J. Aguiomar Foggiatto, D. Coradini Schwarz, The influence of support base on FDM accuracy in Z, *Rapid Prototyp. J.* 20 (2014) 182–191. <https://doi.org/10.1108/RPJ-12-2012-0116>.
- [25] G.P. Kumar, S.P. Regalla, Optimization of Support Material and Build Time in Fused Deposition Modeling (FDM), *Appl. Mech. Mater.* 110–116 (2011) 2245–2251. <https://doi.org/10.4028/www.scientific.net/AMM.110-116.2245>.
- [26] J. Vanek, J. a. G. Galicia, B. Benes, Clever Support: Efficient Support Structure Generation for Digital Fabrication, *Comput. Graph. Forum.* 33 (2014) 117–125. <https://doi.org/10.1111/cgf.12437>.

- [27] S.L. Messimer, A.E. Patterson, N. Muna, A.P. Deshpande, T. Rocha Pereira, Characterization and Processing Behavior of Heated Aluminum-Polycarbonate Composite Build Plates for the FDM Additive Manufacturing Process, *J. Manuf. Mater. Process.* 2 (2018) 12. <https://doi.org/10.3390/jmmp2010012>.
- [28] K. Singh, Experimental study to prevent the warping of 3D models in fused deposition modeling, *Int. J. Plast. Technol.* 22 (2018) 177–184. <https://doi.org/10.1007/s12588-018-9206-y>.
- [29] A.S. de León, A. Domínguez-Calvo, S.I. Molina, Materials with enhanced adhesive properties based on acrylonitrile-butadiene-styrene (ABS)/thermoplastic polyurethane (TPU) blends for fused filament fabrication (FFF), *Mater. Des.* 182 (2019) 108044. <https://doi.org/10.1016/j.matdes.2019.108044>.
- [30] T.-M. Wang, J.-T. Xi, Y. Jin, A model research for prototype warp deformation in the FDM process, *Int. J. Adv. Manuf. Technol.* 33 (2007) 1087–1096. <https://doi.org/10.1007/s00170-006-0556-9>.
- [31] R. Polak, F. Sedlacek, K. Raz, Determination of FDM Printer Settings with Regard to Geometrical Accuracy, in: B. Katalinic (Ed.), *DAAAM Proc.*, 1st ed., DAAAM International Vienna, 2017: pp. 0561–0566. <https://doi.org/10.2507/28th.daaam.proceedings.079>.
- [32] M.S. Alsoufi, A.E. Elsayed, How Surface Roughness Performance of Printed Parts Manufactured by Desktop FDM 3D Printer with PLA+ is Influenced by Measuring Direction, *Am. J. Mech. Eng.* 5 (2017) 211–222. <https://doi.org/10.12691/ajme-5-5-4>.
- [33] R. Singh, S. Singh, I.P. Singh, F. Fabbrocino, F. Fraternali, Investigation for surface finish improvement of FDM parts by vapor smoothing process, *Compos. Part B Eng.* 111 (2017) 228–234. <https://doi.org/10.1016/j.compositesb.2016.11.062>.
- [34] I. Gajdoš, E. Spišák, L. Kaščák, V. Krasinskyi, Surface Finish Techniques for FDM Parts, *Mater. Sci. Forum.* 818 (2015) 45–48. <https://doi.org/10.4028/www.scientific.net/MSF.818.45>.

- [35] N. Jayanth, P. Senthil, C. Prakash, Effect of chemical treatment on tensile strength and surface roughness of 3D-printed ABS using the FDM process, *Virtual Phys. Prototyp.* 13 (2018) 155–163. <https://doi.org/10.1080/17452759.2018.1449565>.
- [36] F. Rayegani, G.C. Onwubolu, Fused deposition modelling (FDM) process parameter prediction and optimization using group method for data handling (GMDH) and differential evolution (DE), *Int. J. Adv. Manuf. Technol.* 73 (2014) 509–519. <https://doi.org/10.1007/s00170-014-5835-2>.
- [37] R. Quelho de Macedo, R.T.L. Ferreira, K. Jayachandran, Determination of mechanical properties of FFF 3D printed material by assessing void volume fraction, cooling rate and residual thermal stresses, *Rapid Prototyp. J.* 25 (2019) 1661–1683. <https://doi.org/10.1108/RPJ-08-2018-0192>.
- [38] A.A. Bakır, R. Atik, S. Özerinç, Effect of fused deposition modeling process parameters on the mechanical properties of recycled polyethylene terephthalate parts, *J. Appl. Polym. Sci.* (2020) 49709. <https://doi.org/10.1002/app.49709>.
- [39] M. Schouten, G. Wolterink, A. Dijkshoorn, D. Kosmas, S. Stramigioli, G. Krijnen, A Review of Extrusion-Based 3D Printing for the Fabrication of Electro- and Biomechanical Sensors, *IEEE Sens. J.* 21 (2021) 12900–12912. <https://doi.org/10.1109/JSEN.2020.3042436>.
- [40] I. Calafel, R.H. Aguirresarobe, M.I. Peñas, A. Santamaria, M. Tierno, J.I. Conde, B. Pascual, Searching for Rheological Conditions for FFF 3D Printing with PVC Based Flexible Compounds, *Materials.* 13 (2020) 178. <https://doi.org/10.3390/ma13010178>.
- [41] M. Vaezi, S. Chianrabutra, B. Mellor, S. Yang, Multiple material additive manufacturing – Part 1: a review, *Virtual Phys. Prototyp.* 8 (2013) 19–50. <https://doi.org/10.1080/17452759.2013.778175>.
- [42] R. Freund, H. Watschke, J. Heubach, T. Vietor, Determination of influencing factors on interface strength of additively manufactured multi-material parts by material extrusion, *Appl. Sci. Switz.* (2019). <https://doi.org/10.3390/app9091782>.

- [43] D. Baca, R. Ahmad, The impact on the mechanical properties of multi-material polymers fabricated with a single mixing nozzle and multi-nozzle systems via fused deposition modeling, *Int. J. Adv. Manuf. Technol.* 106 (2020) 4509–4520. <https://doi.org/10.1007/s00170-020-04937-3>.
- [44] H. Song, J. Martinez, P. Bedell, N. Vennin, S. Lefebvre, Colored fused filament fabrication, *ArXiv170909689 Cs.* (2019). <http://arxiv.org/abs/1709.09689> (accessed July 29, 2021).
- [45] Md.H. Ali, N. Mir-Nasiri, W.L. Ko, Multi-nozzle extrusion system for 3D printer and its control mechanism, *Int. J. Adv. Manuf. Technol.* 86 (2016) 999–1010. <https://doi.org/10.1007/s00170-015-8205-9>.
- [46] L.R. Lopes, A.F. Silva, O.S. Carneiro, Multi-material 3D printing: The relevance of materials affinity on the boundary interface performance, *Addit. Manuf.* 23 (2018) 45–52. <https://doi.org/10.1016/j.addma.2018.06.027>.
- [47] K. Kalia, A. Ameli, Interfacial Bond Strength of Various Rigid/Soft Multi-Materials Printed via Fused Filament Fabrication Process, 2020. <http://asmedigitalcollection.asme.org/SMASIS/proceedings-pdf/SMASIS2020/84027/V001T01A010/6588104/v001t01a010-smasis2020-2298.pdf>.
- [48] L. Rossing, R.B.N. Scharff, B. Chömpff, C.C.L. Wang, E.L. Doubrovski, Bonding between silicones and thermoplastics using 3D printed mechanical interlocking, *Mater. Des.* 186 (2020) 108254. <https://doi.org/10.1016/j.matdes.2019.108254>.
- [49] M.F. Rabbi, V. Chalivendra, Interfacial fracture characterization of multi-material additively manufactured polymer composites, *Compos. Part C Open Access.* 5 (2021) 100145. <https://doi.org/10.1016/j.jcomc.2021.100145>.
- [50] J. Yin, C. Lu, J. Fu, Y. Huang, Y. Zheng, Interfacial bonding during multi-material fused deposition modeling (FDM) process due to inter-molecular diffusion, *Mater. Des.* 150 (2018) 104–112. <https://doi.org/10.1016/j.matdes.2018.04.029>.

- [51] F. Tamburrino, S. Graziosi, M. Bordegoni, The influence of slicing parameters on the multi-material adhesion mechanisms of FDM printed parts: an exploratory study, *Virtual Phys. Prototyp.* 14 (2019) 316–332. <https://doi.org/10.1080/17452759.2019.1607758>.
- [52] J. Hetherington, H. Askes, A mass matrix formulation for cohesive surface elements, *Theor. Appl. Fract. Mech.* 69 (2014) 110–117. <https://doi.org/10.1016/j.tafmec.2013.11.011>.
- [53] M.R. Khosravani, P. Soltani, K. Weinberg, T. Reinicke, Structural integrity of adhesively bonded 3D-printed joints, *Polym. Test.* 100 (2021) 107262. <https://doi.org/10.1016/j.polymertesting.2021.107262>.
- [54] Filaments.directory Tops 2,000 Products and Releases First Trend Report, 3DPrintcom Voice 3D Print. Addit. Manuf. (2016). <https://3dprint.com/131799/filaments-directory-trends/> (accessed July 24, 2021).
- [55] N.G. Tanikella, B. Wittbrodt, J.M. Pearce, Tensile strength of commercial polymer materials for fused filament fabrication 3D printing, *Addit. Manuf.* 15 (2017) 40–47. <https://doi.org/10.1016/j.addma.2017.03.005>.
- [56] Y.C. Ching, T.U. Gunathilake, K.Y. Ching, C.H. Chuah, V. Sandu, R. Singh, N.-S. Liou, Effects of high temperature and ultraviolet radiation on polymer composites, in: *Durab. Life Predict. Biocomposites Fibre-Reinf. Compos. Hybrid Compos.*, Elsevier, 2019: pp. 407–426. <https://doi.org/10.1016/B978-0-08-102290-0.00018-0>.
- [57] E. Kim, Y.-J. Shin, S.-H. Ahn, The effects of moisture and temperature on the mechanical properties of additive manufacturing components: fused deposition modeling, *Rapid Prototyp. J.* 22 (2016) 887–894. <https://doi.org/10.1108/RPJ-08-2015-0095>.
- [58] B. Pinpathomrat, C. Narita, A. Yokoyama, K. Yamada, Evaluation of degradation of ultraviolet-C irradiated polylactic acid/carbon-fiber composites using fluorescence spectroscopy, *Adv. Compos. Mater.* 0 (2021) 1–13. <https://doi.org/10.1080/09243046.2021.1943108>.

- [59] I. Durgun, R. Ertan, Experimental investigation of FDM process for improvement of mechanical properties and production cost, *Rapid Prototyp. J.* 20 (2014) 228–235. <https://doi.org/10.1108/RPJ-10-2012-0091>.
- [60] A. Rodríguez-Panes, J. Claver, A. Camacho, The Influence of Manufacturing Parameters on the Mechanical Behaviour of PLA and ABS Pieces Manufactured by FDM: A Comparative Analysis, *Materials*. 11 (2018) 1333. <https://doi.org/10.3390/ma11081333>.
- [61] M. Samykano, S.K. Selvamani, K. Kadirgama, W.K. Ngui, G. Kanagaraj, K. Sudhakar, Mechanical property of FDM printed ABS: influence of printing parameters, *Int. J. Adv. Manuf. Technol.* 102 (2019) 2779–2796. <https://doi.org/10.1007/s00170-019-03313-0>.
- [62] F. Carrasco, P. Pagès, J. Gámez-Pérez, O.O. Santana, M.L. MasPOCH, Processing of poly(lactic acid): Characterization of chemical structure, thermal stability and mechanical properties, *Polym. Degrad. Stab.* 95 (2010) 116–125. <https://doi.org/10.1016/j.polymdegradstab.2009.11.045>.
- [63] R.E. Drumright, P.R. Gruber, D.E. Henton, Polylactic Acid Technology, *Adv. Mater.* 12 (2000) 1841–1846. [https://doi.org/10.1002/1521-4095\(200012\)12:23<1841::AID-ADMA1841>3.0.CO;2-E](https://doi.org/10.1002/1521-4095(200012)12:23<1841::AID-ADMA1841>3.0.CO;2-E).
- [64] B. Kaygusuz, S. Özerinç, Improving the ductility of polylactic acid parts produced by fused deposition modeling through polyhydroxyalkanoate additions, *J. Appl. Polym. Sci.* 136 (2019) 48154. <https://doi.org/10.1002/app.48154>.
- [65] A.P. Valerga, M. Batista, J. Salguero, F. Girot, Influence of PLA Filament Conditions on Characteristics of FDM Parts, *Materials*. 11 (2018) 1322. <https://doi.org/10.3390/ma11081322>.
- [66] M. Algarni, The Influence of Raster Angle and Moisture Content on the Mechanical Properties of PLA Parts Produced by Fused Deposition Modeling, *Polymers*. 13 (2021) 237. <https://doi.org/10.3390/polym13020237>.

- [67] Q. Sun, G.M. Rizvi, C.T. Bellehumeur, P. Gu, Effect of processing conditions on the bonding quality of FDM polymer filaments, *Rapid Prototyp. J.* 14 (2008) 72–80. <https://doi.org/10.1108/13552540810862028>.
- [68] M.V. Podzorova, Yu.V. Tertyshnaya, P.V. Pantyukhov, A.A. Popov, S.G. Nikolaeva, Influence of ultraviolet on polylactide degradation, in: Tomsk, Russia, 2017: p. 020173. <https://doi.org/10.1063/1.5013854>.
- [69] H.J. Qi, M.C. Boyce, Stress–strain behavior of thermoplastic polyurethanes, *Mech. Mater.* 37 (2005) 817–839. <https://doi.org/10.1016/j.mechmat.2004.08.001>.
- [70] J. Leng, J. Wu, J. Zhang, Preparation of Thermoplastic Polyurethane Parts Reinforced with in Situ Polylactic Acid Microfibers during Fused Deposition Modeling: The Influences of Deposition-Induced Effects, *Ind. Eng. Chem. Res.* 58 (2019) 21476–21484. <https://doi.org/10.1021/acs.iecr.9b04285>.
- [71] V. Mazzanti, L. Malagutti, F. Mollica, FDM 3D Printing of Polymers Containing Natural Fillers: A Review of their Mechanical Properties, *Polymers.* 11 (2019) 1094. <https://doi.org/10.3390/polym11071094>.
- [72] J. Xiao, Y. Gao, The manufacture of 3D printing of medical grade TPU, *Prog. Addit. Manuf.* 2 (2017) 117–123. <https://doi.org/10.1007/s40964-017-0023-1>.
- [73] W.D. Callister, J.G. David Rethwisch, *MATERIALS SCIENCE and ENGINEERING*, n.d.
- [74] T.N.A. Tuan Rahim, A.M. Abdullah, H. Md Akil, D. Mohamad, Z.A. Rajion, Preparation and characterization of a newly developed polyamide composite utilising an affordable 3D printer, *J. Reinf. Plast. Compos.* 34 (2015) 1628–1638. <https://doi.org/10.1177/0731684415594692>.
- [75] S. Kumar, R. Singh, T. Singh, A. Batish, Fused filament fabrication: A comprehensive review, *J. Thermoplast. Compos. Mater.* (2020) 089270572097062. <https://doi.org/10.1177/0892705720970629>.
- [76] Y. Jia, H. He, X. Peng, S. Meng, J. Chen, Y. Geng, Preparation of a new filament based on polyamide-6 for three-dimensional printing, *Polym. Eng. Sci.* 57 (2017) 1322–1328. <https://doi.org/10.1002/pen.24515>.

- [77] V.C. Gavali, P.R. Kubade, H.B. Kulkarni, Mechanical and Thermo-mechanical Properties of Carbon fiber Reinforced Thermoplastic Composite Fabricated Using Fused Deposition Modeling Method, *Mater. Today Proc.* 22 (2020) 1786–1795. <https://doi.org/10.1016/j.matpr.2020.03.012>.
- [78] F. Ning, W. Cong, J. Qiu, J. Wei, S. Wang, Additive manufacturing of carbon fiber reinforced thermoplastic composites using fused deposition modeling, *Compos. Part B Eng.* 80 (2015) 369–378. <https://doi.org/10.1016/j.compositesb.2015.06.013>.
- [79] G. Liao, Z. Li, Y. Cheng, D. Xu, D. Zhu, S. Jiang, J. Guo, X. Chen, G. Xu, Y. Zhu, Properties of oriented carbon fiber/polyamide 12 composite parts fabricated by fused deposition modeling, *Mater. Des.* 139 (2018) 283–292. <https://doi.org/10.1016/j.matdes.2017.11.027>.
- [80] M.F. Arif, H. Alhashmi, K.M. Varadarajan, J.H. Koo, A.J. Hart, S. Kumar, Multifunctional performance of carbon nanotubes and graphene nanoplatelets reinforced PEEK composites enabled via FFF additive manufacturing, *Compos. Part B Eng.* 184 (2020) 107625. <https://doi.org/10.1016/j.compositesb.2019.107625>.
- [81] W. Zhang, C. Cotton, J. Sun, D. Heider, B. Gu, B. Sun, T.-W. Chou, Interfacial bonding strength of short carbon fiber/acrylonitrile-butadiene-styrene composites fabricated by fused deposition modeling, *Compos. Part B Eng.* 137 (2018) 51–59. <https://doi.org/10.1016/j.compositesb.2017.11.018>.
- [82] K. Dong, L. Liu, X. Huang, X. Xiao, 3D printing of continuous fiber reinforced diamond cellular structural composites and tensile properties, *Compos. Struct.* 250 (2020) 112610. <https://doi.org/10.1016/j.compstruct.2020.112610>.
- [83] M. Heidari-Rarani, M. Rafiee-Afarani, A.M. Zahedi, Mechanical characterization of FDM 3D printing of continuous carbon fiber reinforced PLA composites, *Compos. Part B Eng.* 175 (2019) 107147. <https://doi.org/10.1016/j.compositesb.2019.107147>.

- [84] N. Li, Y. Li, S. Liu, Rapid prototyping of continuous carbon fiber reinforced polylactic acid composites by 3D printing, *J. Mater. Process. Technol.* 238 (2016) 218–225. <https://doi.org/10.1016/j.jmatprotec.2016.07.025>.
- [85] I. Ferreira, D. Vale, M. Machado, J. Lino, Additive manufacturing of polyethylene terephthalate glycol /carbon fiber composites: An experimental study from filament to printed parts, *Proc. Inst. Mech. Eng. Part J. Mater. Des. Appl.* 233 (2019) 1866–1878. <https://doi.org/10.1177/1464420718795197>.
- [86] E. Verdejo de Toro, J. Coello Sobrino, A. Martínez Martínez, V. Miguel Eguía, J. Ayllón Pérez, Investigation of a Short Carbon Fibre-Reinforced Polyamide and Comparison of Two Manufacturing Processes: Fused Deposition Modelling (FDM) and Polymer Injection Moulding (PIM), *Materials*. 13 (2020) 672. <https://doi.org/10.3390/ma13030672>.
- [87] H.L. Tekinalp, V. Kunc, G.M. Velez-Garcia, C.E. Duty, L.J. Love, A.K. Naskar, C.A. Blue, S. Ozcan, Highly oriented carbon fiber–polymer composites via additive manufacturing, *Compos. Sci. Technol.* 105 (2014) 144–150. <https://doi.org/10.1016/j.compscitech.2014.10.009>.
- [88] B. Brenken, E. Barocio, A. Favaloro, V. Kunc, R.B. Pipes, Fused filament fabrication of fiber-reinforced polymers: A review, *Addit. Manuf.* 21 (2018) 1–16. <https://doi.org/10.1016/j.addma.2018.01.002>.
- [89] Standard Test Method for Tensile Properties of Plastics, ASTM D638-14, 2015.
- [90] Standard Test Methods for Vulcanized Rubber and Thermoplastic Elastomers - Tension, ASTM D412-16, 2016.
- [91] H. Dal, K. Açıkgöz, Y. Badienia, On the Performance of Isotropic Hyperelastic Constitutive Models for Rubber-Like Materials: A State of the Art Review, *Appl. Mech. Rev.* 73 (2021). <https://doi.org/10.1115/1.4050978>.
- [92] R.W. Ogden, G. Saccomandi, I. Sgura, Fitting hyperelastic models to experimental data, *Comput. Mech.* 34 (2004) 484–502. <https://doi.org/10.1007/s00466-004-0593-y>.
- [93] Standard Test Method for Compressive Properties of Rigid Cellular Plastics, ASTM D1621-16, 2016.

- [94] E.B. Duoss, T.H. Weisgraber, K. Hearon, C. Zhu, W. Small, T.R. Metz, J.J. Vericella, H.D. Barth, J.D. Kuntz, R.S. Maxwell, C.M. Spadaccini, T.S. Wilson, Three-Dimensional Printing of Elastomeric, Cellular Architectures with Negative Stiffness, *Adv. Funct. Mater.* 24 (2014) 4905–4913. <https://doi.org/10.1002/adfm.201400451>.
- [95] F.N. Habib, P. Iovenitti, S.H. Masood, M. Nikzad, Fabrication of polymeric lattice structures for optimum energy absorption using Multi Jet Fusion technology, *Mater. Des.* 155 (2018) 86–98. <https://doi.org/10.1016/j.matdes.2018.05.059>.
- [96] M. Avalle, G. Belingardi, R. Montanini, Characterization of polymeric structural foams under compressive impact loading by means of energy-absorption diagram, *Int. J. Impact Eng.* 25 (2001) 455–472. [https://doi.org/10.1016/S0734-743X\(00\)00060-9](https://doi.org/10.1016/S0734-743X(00)00060-9).